[American Journal of Science, Vol. 321, October, 2021, P. 1204–1245, DOI 10.2475/08.2021.03]

QUANTIFYING BIOTIC AND ABIOTIC SI FLUXES IN THE CRITICAL ZONE WITH GE/SI RATIOS ALONG A GRADIENT OF EROSION RATES

PATRICK J. FRINGS*,†, FRANZISKA SCHUBRING*, MARCUS OELZE*, and FRIEDHELM VON BLANCKENBURG*,**

ABSTRACT. Silicon (Si) is an important nutrient for many plant and algae species, and the ultimate source of Si is silicate mineral weathering reactions. These topics have inspired the application of Si isotope geochemistry to quantifying Si cycling in the Critical Zone, though the interpretations are often equivocal. Because germanium (Ge) geochemistry is similar to that of Si, the Ge/Si ratio is considered a tracer that provides additional constraints on Si cycling. Here, we provide Ge/Si ratios for three sites that span a gradient of erosion rates and thus time that material spends in the weathering zone before being removed. We present Ge/Si ratios in bulk rock, soil and saprolite, clay-size fractions, plant biomass, and river water from the Central Swiss Alps, the southern Californian Sierra Nevada, and the highlands of Sri Lanka. Our data perform two functions. First, they provide insight into the Ge/Si system. In particular, we document the presence of a substantial pool of Ge in plant biomass that is not associated with phytoliths, suggesting that overall plants do not discriminate against Ge relative to Si during uptake. We also quantify the preferential incorporation of Ge into clay minerals. We show that Ge/Si ratios in secondary clays may be a better proxy for weathering intensity (the fraction of denudation achieved chemically) than the Ge/Si ratio of river solutes. Ge/Si ratios in secondary clay minerals also perform as well as or even better than silicon isotopes as weathering intensity proxies. Second, the Ge/Si data are used in conjunction with silicon isotope data to develop a catchment Si mass-balance model. It suggests that the export of secondary, fractionated solids (largely clays and plant material) becomes increasingly important at shorter regolith residence times: 80^{+15}_{-24} % of total solubilized Si in the rapidly eroding Alps site, vs. 32^{+22}_{-20} % in the slowly eroding Sri Lanka site. The results also suggest that plant material is a surprisingly large contributor to Si export from these catchments, likely equivalent to 25 to110 % of dissolved Si export.

INTRODUCTION

The weathering of silicate rocks is coupled to the carbon cycle by the sequestration of CO_2 (Berner and others, 1983; Frings, 2019) and through the supply of mineral nutrients, amongst them silicon (Si). In broad strokes, the main pathways in the terrestrial Si cycle are well known. Si is released from the primary minerals comprising bedrock during weathering as dissolved silica (dSi, typically as the neutral species monosilicic acid H_4SiO_4). This dSi has several potential fates. It can be transported directly to the fluvial system via groundwater or soil water flow. It may be precipitated or adsorbed into secondary phases, including the clay minerals and various oxides or amorphous and short-range order phases. Finally, it may be taken up by plants or soil organisms to produce biogenic silica (bSi; hydrated amorphous SiO_2) (Alexandre and others, 1997; Sommer and others, 2006; Carey and Fulweiler, 2012). All these phases may be further redissolved, recycled, or geochemically altered before the Si is ultimately transported by rivers to the ocean as dSi or as eroded particulates.

* GFZ German Research Centre for Geosciences, Section Earth Surface Geochemistry, Telegrafenberg, 14473 Potsdam, Germany
** Also at Institute of Geological Sciences, Freie Universität Berlin, 12249 Berlin, Germany
† Corresponding author: patrick.frings@gfz-potsdam.de

Biological Si utilisation is increasingly recognised as a central part of terrestrial Si cycling (for example, Meunier and others, 1999; Gerard and others, 2008). Though not strictly bio-essential, Si provides benefits for many vascular plants. For example, it can provide physiological and structural advantages, or convey resistance to herbivory (Ma and others, 2001; Pilon-Smits and others, 2009; Guntzer and others, 2012), and so some plant taxa actively accumulate Si. In other cases, it may simply be taken up passively. Upon plant death or leaf abscission, plant bSi is returned to the soil system where is may be stored, be eroded, or redissolve to produce dSi. Si uptake by biomass is often of the same order of magnitude or greater than Si release during weathering (Conley, 2002; Carey and Fulweiler, 2012), so terrestrial ecosystems can be conceptualised as a buffer between silicate weathering and the ultimate delivery of Si to the ocean (Derry and others, 2005). There is a sizable body of literature examining Si budgets and fluxes within ecosystems (Conley, 2002; Clymans and others, 2016; de Tombeur and others 2020), or the storage of phytoliths in soils (for example, Meunier and others, 1999; Li and others, 2020). Despite this, the removal of plant bSi via erosion has not received much attention. Nevertheless, export of plant material may be a non-negligible component of many element budgets (for example, Oeser and von Blanckenburg 2020; Bouchez and von Blanckenburg, 2021; von Blanckenburg and others, 2021).

Geochemical tools are a promising means of characterising the Si cycle in the Critical Zone – the layer of the Earth surface that extends from the bottom of groundwater to the tops of trees (Brantley and others, 2007). In particular, Si isotope ratios are well established (De La Rocha and others, 2000; Ziegler and others, 2005a, 2005b; Opfergelt and Delmelle, 2012; Frings and others, 2015, 2016). Expressed as δ^{30}Si (a permil deviation in the ^{30}Si/^{28}Si ratio from the reference material NBS28), they have been extensively used to trace aspects of Critical Zone Si cycling. The approach benefits from the observation that Si isotope ratios in bulk igneous silicate rocks are reasonably consistent, falling around δ^{30}Si = -0.23 ± 0.15 ‰ (Savage and others, 2013a). In contrast, biotic and abiotic formation of solids creates a range of over 10 ‰ in Earth surface δ^{30}Si (Frings and others, 2016). Both sequestration of Si into secondary minerals and Si uptake by plants favour the incorporation of the lighter Si isotopes. Both therefore require a residual dSi pool enriched in ^{30}Si. This is found in soil- and stream waters that are almost exclusively higher than bedrock values (δ^{30}Si between -0.1 and $+4.66$ ‰; values compiled in Frings and others (2016)). Since Si isotope fractionations associated with both processes result in lighter δ^{30}Si values in the new solids relative to the source material, Si isotope ratios alone cannot sufficiently resolve which of the two processes governs river δ^{30}Si, limiting its potential as a weathering or nutrient cycling tracer.

To distinguish between plant uptake and clay formation, germanium/silicon ratios (Ge/Si, expressed in μmol mol^{-1}) are a potentially complementary tool (Kurtz and others, 2002; Derry and others, 2005; Scribner and others, 2006; Blecker and others, 2007; Opfergelt and others, 2010). Ge and Si are both group IV elements and have similar geochemical characteristics. In particular, they have the same outer electron structure and similar bond lengths in Ge-O (1.75 Å) and Si-O (1.64 Å) tetrahedra, which allow the substitution of Si by Ge in silicate minerals (Goldschmidt, 1926; Martin and others, 1996). Indeed, germanium is often described as a "pseudoisotope" of Si (for example, Kurtz and others, 2002), which 'fractionates' (partitions) relative to Si at the Earth Surface.

One of the first usages of Ge/Si ratios was as a proxy for weathering intensity – the fraction of denudation accomplished chemically (Murnane and Stallard, 1990). Subsequent work (for example, Froelich and others, 1992; Baronas and others, 2018) related Ge/Si ratios to the stochiometry of net weathering reactions. For most silicate

rocks the Ge/Si ratio lies around 2 μmol mol^{-1} (De Argollo and Schilling, 1978; Bernstein, 1985; Lugolobi and others, 2010). Ge/Si ratios in secondary clay minerals are typically higher (> 4 μmol mol^{-1}), reflecting the preferential partitioning of Ge relative to Si into them. As with δ^{30}Si, a complementary low Ge/Si pool is required by mass-balance: this is also found in river solutes, which typically have lower Ge/Si (< 1 μmol mol^{-1}) than the source rock (Froelich and others, 1985; Mortlock and Froelich, 1987). Riverine Ge/Si thus reflects the partitioning of Ge relative to Si into secondary phases, which in itself reflects weathering intensity. River Ge/Si ratios also have the benefit – and complication – of integrating over the whole Critical Zone. In general, low intensity settings produce low dissolved Ge/Si (most Ge in clays) while higher-intensity settings produce higher dissolved Ge/Si (closer to parent material ratios, when soils are more highly leached) (Murnane and Stallard, 1990; Kurtz and others, 2002).

One putative benefit of Ge/Si ratios over Si isotopes is that plants are thought to discriminate against Ge: almost all available data show that phytoliths separated from plant biomass have low Ge/Si ratios, and so plants are thought to discriminate against Ge during Si uptake (Kurtz and Derry, 2004; Derry and others, 2005; Blecker and others, 2007; Delvigne and others, 2009; Cornelis and others, 2010; Lugolobi and others, 2010; White and others, 2012; Meek and others, 2016). Because this is opposite in direction to the partitioning of Ge into clays, a combination of Ge/Si ratios and δ^{30}Si may yield insights into Si cycling in a way that either alone cannot.

Yet several issues surrounding the interpretation of Ge/Si ratios remain unaddressed. For example, Lugolobi and others (2010) report that Ge/Si ratios of primary minerals vary from 0.5 (quartz) to > 5 μmol mol^{-1} (biotite and hornblende). Ge substitution for Si thus appears to decrease with the degree of linkage in the crystallographic structure of the mineral (Bernstein, 1985; Lugolobi and others, 2010). This implies that preferential dissolution of some primary minerals may produce a solute Ge/Si ratio that differs from the bulk rock during initial weathering in sites where only some of the minerals dissolve before being lost to erosion. Additionally, most plant Ge/Si determinations to date have been made on phytolith separates rather than bulk plants, but a recent determination of a Ge bulk concentration yielded 70 ng g^{-1} in the Rye Grass standard (ERM-CD281; Delvigne and others, 2018). Coupled with the recommended value for Si mass fraction in Rye Grass (1.3 g kg^{-1}), this produces a Ge/Si ratio of *ca.* 20.8 μmol mol^{-1}. Thus at least some plants have Ge/Si ratios much greater than typical phytolith values of <1 μmol mol^{-1} (Derry and others, 2005). Elsewhere, hydroponic experiments show no sign of discrimination during uptake by banana plantlets (Delvigne and others, 2009). Together, this challenges the assumption of Ge discrimination relative to Si during plant uptake. Finally, the controls on the extent to which Ge is preferentially partitioned into clay minerals in natural systems is poorly understood, and the range of magnitudes of this preferential partitioning experienced in natural systems is wide and poorly delimited. These parameters are a fundamental part of any interpretative framework.

To improve the interpretational framework for Ge/Si ratios, and to show how a combination of Ge/Si and δ^{30}Si can be used to quantify the continental Si cycle we investigate Ge and Si partitioning in bulk soil and saprolite (chemically altered rock), the clay-sized fraction, plants, and waters at three different field sites (named 'Alps', 'Sierra Nevada', and 'Sri Lanka'). The field site in Sri Lanka represents a supply-limited regime: erosion rates are low and the supply of fresh weatherable minerals is the factor that limits weathering rates. The Alps site represents a kinetically limited regime, where mineral supply rates are sufficiently high that dissolution kinetics limit weathering rates. The field site in the Sierra Nevada displays an intermediate weathering regime. Each of these field sites is underlain by similar felsic rocks and is well characterised, with minimal anthropogenic influence. The three sites constitute an

TABLE 1

Main characteristics of the three study sites

	Alps	Sierra Nevada	Sri Lanka
Profile depth (cm)	35	700	1000
Denudation rate (t km^{-2} yr^{-1})[a]	103±40	22±56	42±6.4
Denudation rate (mm kyr^{-1})[b]	38.1±15	81.9±21	15.4±2.3
Mean CDF	0.31±0.21	0.36±0.09	0.5±0.15
Weathering rate (t km^{-2} yr^{-1})	32±25	80	20.8
Erosion rate (t km^{-2} yr^{-1})	71±55	141	20.8
Regolith Residence time (kyr)[c]	~10	~86	~600
Weathering regime	Kinetically limited	Intermediate	Supply limited

Data and uncertainties (expressed as $\pm$ 1 σ) from von Blanckenburg and others (2021). [a]Assumed equal to regolith production rates (see von Blanckenburg and others, 2021 for details). [b]Calculated assuming a bedrock density of 2.7 t m^{-3}. [c]Calculated assuming regolith thicknesses of about 0.4, 7.0 and 9.2 m.

'erodosequence' (see details in von Blanckenburg and others, 2021). This is a powerful approach for the 'calibration' of novel isotope or elemental ratios. Primary mineral persistence, secondary mineral formation, the physical architecture of the Critical Zone, and ecosystem functioning, are all related to regolith residence time that translates into weathering intensity (von Blanckenburg and others, 2021). This erodosequence thus provides the opportunity to examine the behaviour of novel geochemical tools in different weathering settings. Eroding sites have the advantage of behaving as geochemical flow-through reactors (Lebedeva and others, 2010; Bouchez and others, 2013) so that simple mass-balance models can be applied.

Here, we show that Ge/Si ratios in clay minerals are a useful proxy for the weathering intensity of a site. However, we also show that the potential of Ge/Si ratios as a tool to distinguish between Si sequestration into secondary minerals and the Si taken up by plants is not as straightforward as previously thought. We use these insights to create a Ge/Si-δ^{30}Si mass balance model that suggests an important role for biology in terrestrial Si cycling.

STUDY SITES

The main characteristics of each site are summarized below and in table 1. Figure 1 shows the geographical setting of the three sites. Detailed descriptions of the Alps, Sierra Nevada and Sri Lanka sites are given in Norton and von Blanckenburg (2010), Uhlig and others (2017), and Hewawasam and others (2013), respectively. von Blanckenburg and others (2021) present a comparison of the key physical and geochemical characteristics of the sites, the erosion, weathering, and elemental ecosystem fluxes, key features of sample locations and detailed sampling strategies.

Alps

The site is located in the Swiss Central Alps on a soil mantled ridge in the Upper Rhone valley at an altitude of 2565 m (Figure 1A). Mean annual precipitation is about 1140 mm yr^{-1} and mean temperatures are 3.1 °C (as recorded at Ulrichen in the Gorn at 1345 m altitude). No saprolite is present and soils are thin (< 50 cm). Bedrock is the Aare Massif, which is mainly foliated gneiss (modal mineralogical composition of 23 % quartz, 53 % plagioclase, 17 % orthoclase, 4 % biotite and 3 % muscovite) and granite (34 % quartz, 35 % plagioclase, 27 % orthoclase and 4 % biotite).

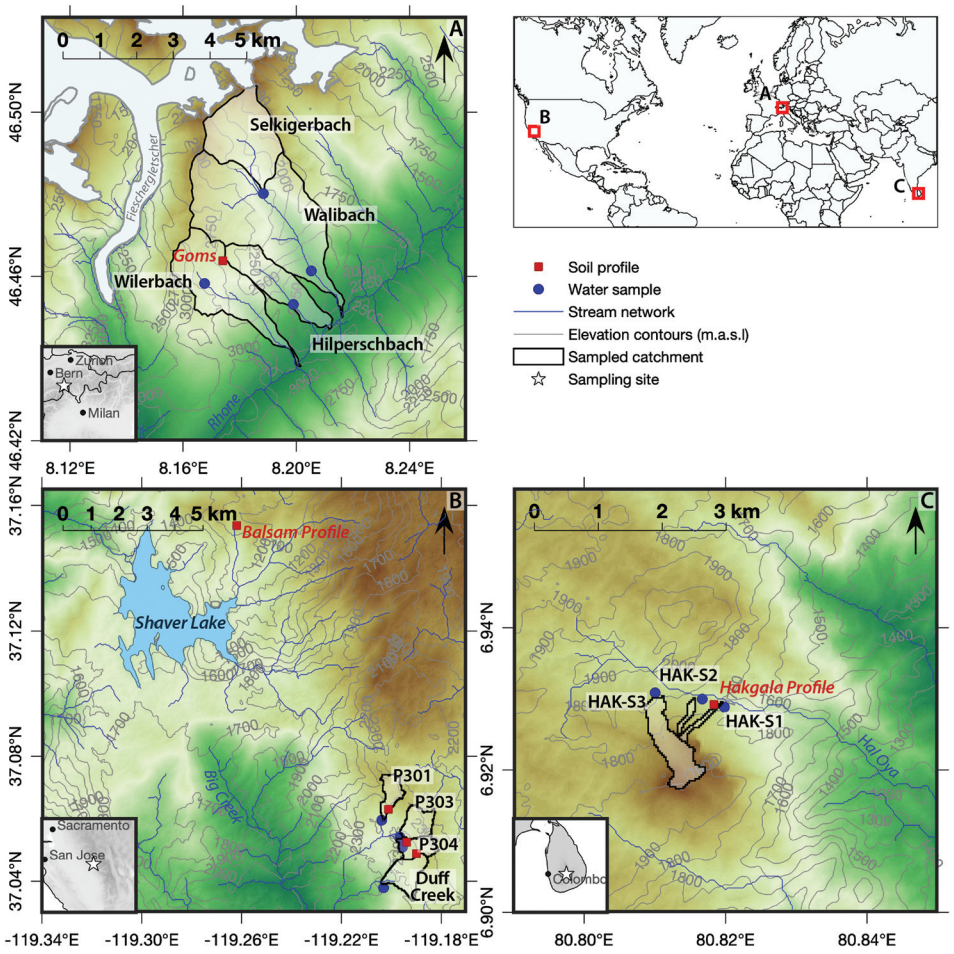

Figure 1. Locations of the three study sites defining our 'erodosequence', and specific sampling sites. A: Alps; B. Sierra Nevada; C. Sri Lanka. More details are given in the main text and in von Blanckenburg and others (2021).

Soils are mostly organic rich podzols (Egli and others, 2008), and contain both secondary clay minerals and unweathered primary minerals.

A mean denudation rate of 103 t km^{-2} yr^{-1} (31.1 mm kyr^{-1}) was estimated from *in situ* ^{10}Be (Norton and others, 2010). A mean chemical depletion fraction (CDF, a zirconium based weathering index after Riebe and others, 2003) of 0.31 implies chemical weathering rates of 32 t km^{-2} yr^{-1} and erosion rates of 71 t km^{-2} yr^{-1}. The resulting regolith residence time is 10 kyr.

Sierra Nevada

Samples come from the Critical Zone Observatory (CZO) Kings River Experimental Watersheds (KREW) in the Southern Sierra Nevada mountain range (fig. 1B). Catchments in the KREW range in size between 0.49 to 1.32 km^2 and are located at altitudes between 1479 and 2113 m, with precipitation of 750 to 2000 mm yr^{-1} (Hunsaker and Neary, 2012). Mean annual temperature is 7.8 °C (Liu and others, 2013). Different soil profiles were sampled within catchments located at the

Providence Creek (P301, P303, P304) and are underlain by the Dinkey Creek granodiorite and the Blue Canyon quartz diorite unit, noted as (Bateman and Wones, 1972). The soils in these catchments are well drained, dominated by a coarse-loamy, mixed soil ("Shaver soil series") and have an organic rich soil horizon. The weathering of feldspars at this site produces kaolinite (Dahlgren and others, 1997; Aguirre, ms, 2019). A deep regolith profile – 'Balsam profile' – located to the northeast of Shaver Lake and about 12 km northwest of the observatory was also sampled. This profile is underlain by the same Dinkey Creek foliated granodiorite. This contains quartz (22.9 vol %), plagioclase (48.1 vol %) and K-feldspar (10 vol %) as major minerals, with others including biotite, hornblende, sphene, apatite and ilmenite making up the remainder (data from Bateman and Wones, 1972). The Blue Canyon quartz diorite is reported to be compositionally similar. See also USGS Geologic Quadrangle Maps GQ-1271 and GQ-987.

Mean *in situ* ^{10}Be denudation rates of 221 t km^{-2} yr^{-1} (81.5 mm kyr^{-1}) and a mean CDF of 0.36 (Dixon and others, 2009) yield weathering rates of 80 t km^{-2} yr^{-1} and erosion rates of 141 t km^{-2} yr^{-1}. The corresponding regolith residence time is 90 kyr (von Blanckenburg and others, 2021).

Sri Lanka

The Hakgala profile is located on a hillslope in the tectonically inactive central Highlands of Sri Lanka at 1753 m altitude (Figure 1C). It is influenced by monsoonal precipitation (2000 mm yr^{-1}) and a mean annual temperature of 16 °C. Local bedrock is charnockite with a SiO_2 content of $>$ 65 %, with K-feldspar (32 %), quartz (30 %), plagioclase (25 %) as the major mineral components, and biotite (7 %) and orthopyroxene (4 %) as minor components. The profile has a depth of more than 10 m. From bedrock to 8 m depth, charnockite corestones with early weathering features are present. Charnockite blocks with of diameter of up to 50 cm occur in the 6 to 8 m section of the profile. In the soil and saprolite, quartz, goethite and kaolinite are the only quantitatively important minerals. The saprolite is blanketed by a red-yellow lateritic soil that supports a natural tropical forest with a thick canopy (Hewawasam and others, 2013).

Denudation rates estimated from *in situ* ^{10}Be average 42 t km^{-2} yr^{-1} (15.4 mm kyr^{-1}) (Hewawasam and others, 2013). A mean CDF of 0.5 was determined (see von Blanckenburg and others, 2021 for details), producing weathering rates of 21 t km^{-2} yr^{-1} and erosion rates of 21 t km^{-2} yr^{-1}. The low denudation rates, coupled with the thick regolith, imply a residence time of *ca.* 600 kyr.

MATERIALS AND METHODS

Sampling.—A detailed description of the sampling strategy is given in von Blanckenburg and others (2021), including profile photos and sketches, and further background data. Below, we outline the key points.

Alps.—Soil profiles were sampled on the soil-mantled ridge top from a 4 m^2 area to decrease site specific variations. Where possible, soil samples were taken from below the organic rich horizon. Some soil samples contained up to 10 % by volume cm-scale rock fragments. All soil samples were sieved at 1 cm and then oven dried at 60°C. Parts of different plant species were taken and oven dried at 60°C. Water samples were filtered using 0.22 µm-porosity PES (polyethersulfone) filter membranes and stored in pre-cleaned PE bottles after acidifying with HNO_3 to a pH of 2.

Sierra Nevada.—Soil samples were taken as depth profiles. In catchment P303 in the KREW a depth profile from the surface to 30 cm was sampled with a soil corer. Samples from different profiles for a specific depth were amalgamated. Samples from Balsam profile were taken from 178 cm to 688 cm depth, so the profile starts at the

soil/saprolite interface and ends at the saprolite/bedrock interface. Parts of different plant species were taken and oven dried at 60°C. Water samples from the Providence Creek were taken as described above.

Sri Lanka.—From a vertical section of the exposed regolith profile at Hakgala, 2 soil and 23 saprolite samples (each *ca.* 500 g) were taken. About 10 m upslope, nine extra soil samples were collected using a soil corer to sample three parallel profiles that were located *ca.* 1.5 m apart. Three depth intervals were integrated (0 to 20 cm, 20 to 40 cm, 40 to 60 cm) by mixing each depth interval with the corresponding depth interval of the other profiles. Water samples from three streams draining catchments adjacent to the profile at Hakgala were collected as above. Fragments from various plant species were collected and oven dried at 60 °C.

Clay Size Fraction Separation

Laboratory work mostly follows Frings and others (2021a) and is only described briefly here. An amorphous Si fraction was leached from ~500 mg sample material in 0.2 M NaOH at 80 °C in a water bath for 5 hours (Sauer and others, 2006), after which the solution and sample were separated by filtration (0.2 µm polyethersulfone syringe filter). A clay-size separation by differential settling in a centrifuge performed on the residual material (USGS protocol OFR01–041). The settling was performed only once to obtain a relatively pure fraction, rather than an estimate of the total clay mass. The amorphous fraction was analysed for its Si isotope composition (Frings and others, 2021a) but Ge/Si ratios are not reported here. We expect the removal of the amorphous phase prior to clay separation to have negligible impact on Ge/Si ratios of the clays, since a) the Si mass fraction in the amorphous fraction is low, and b) initial analyses of a subset of samples showed Ge/Si ratios were similar to the clay size fraction. Clay size separates were combusted in silver crucibles at 700 °C for ≥ 2 hours to remove organic residue, after which 3 ml of 1.6 M NaOH (about 190 mg NaOH total) solution was added to each crucible. This solution was evaporated and then the NaOH coating on the walls and base of the crucible used for an alkaline fusion as detailed below. The clay aliquots were analysed for their Si isotope composition (Frings and others, 2021a) and their Ge/Si ratios (below).

Solid Sample Digestion

All solid samples (bulk soil and saprolite, and plants) were dried and ground. Plant samples were washed with Milli-Q water prior to drying and grinding. Samples were digested by alkaline fusion with sodium hydroxide (NaOH) following Georg and others (2006). Briefly, 5 to 20 mg (bulk soils/saprolites) or 50 to 500 mg (plant material) were combusted by ramped heating (2 hours at 200 °C and 4 hours at 650 °C) in silver crucibles to remove organic material. Subsequently, about 400 mg of high purity NaOH was added, the crucibles capped and heated for 15 min at 750 °C. After cooling, the fusion cake was dissolved in Milli-Q water and 0.03 M HCl and acidified with concentrated HCl to a pH of *ca.* 1.5. Si concentrations in the final sample solutions were kept below 30 µg g^{-1} to avoid silica precipitation. Reference materials (NBS28, BHVO-2, Diatomite) and procedural blanks were processed simultaneously.

Si and Ge Purification and Analysis

The procedures exploit the recent demonstration that Ge and Si remain unfractionationed during the protocols used to purify Si for δ^{30}Si analysis (Delvigne and others, 2018). The advantage is that Ge concentrations can then be readily determined on an ICP-MS with perfectly matrix matched standards at a high throughput rate. Water samples were pre-concentrated by partial evaporation in Teflon beakers at

110 °C (taking care to avoid potential precipitation of Si above 30 μg g^{-1}). Purification of Si and Ge from solutions was adapted from the cation exchange protocol of Georg and others (2006). Because of the similar chemical behaviour of Si and Ge, both are present in solution as the uncharged molecules silicic acid and germanic acid, respectively, at low to neutral pH and therefore do not interact with cation-exchange resin. 1.5 ml of DOWEX 50WX8 (200–400 mesh) resin was used to retain sodium and other cations, while Si and Ge are completely eluted with Milli-Q water (Delvigne and others, 2018).

Most previous Ge/Si determinations have been made by isotope-dilution hydride-generation ICP-MS (Mortlock and Froelich, 1996; Kurtz and others 2002; Derry and others, 2005; Kurtz and others, 2011; Meek and others, 2016) for Ge and ICP-OES or colorimetry for Si. Here, we use a single collector quadrupole ICP-MS (iCAP Q; Thermo-Fisher, Bremen) equipped with a collision cell for the removal of polyatomic interferences. The samples are introduced to the instrument as a wet aerosol from samples in 0.3M HNO_3 and between 2 and 10 μg g^{-1} Si. For each set of samples, we prepared a set of gravimetrically prepared, matrix-matched calibration standards with a single, matching Si concentration (between 2 and 6 μg g^{-1}) but varying Ge concentrations (molar Ge/Si ratios between 0–10 μmol mol^{-1}). From these standards, a calibration regression relating sample Ge/Si ratio was defined from the measured beam intensities. In other words, we directly obtain a Ge/Si ratio rather than two independent concentrations. The isotopes ^{74}Ge and ^{29}Si were integrated 300 times for 0.1 s, and Ge/Si ratios calculated directly from the ratio of beam intensities. The isotope ^{29}Si was monitored in 'high' resolution mode to lower the count rate. Polyatomic interferences (for example, $^{36}Ar^{38}Ar$ on ^{74}Ge) were removed by a collision cell with He as reaction gas, at a flow rate of 5 L min^{-1}. We also monitored ^{70}Ge (20 at%) and ^{72}Ge (27 at%), for 0.01 s integrations. We observed excellent correlations between the ^{70}Ge, ^{72}Ge and ^{74}Ge intensities, and natural abundance ratios, suggesting no isobaric or polyatomic interferences during measurement. The collision cell reduced background counts on a 0.3M HNO_3 matrix to typically < 2 cps on ^{74}Ge. Regression of the standard Ge/Si ratios with the measured ratio of beam intensities produced precise and accurate calibration curves ($r^2 > 0.99$). The secondary reference materials BHVO-2 (literature molar Ge/Si = 2.65 μmol mol^{-1}), BIR-1a (literature Ge concentration = 1.46 μg g^{-1}) and NBS28 were interspersed with unknown samples. The limit of detection with this instrumental protocol is about 0.4 pg g^{-1} Ge. An internal standard (1 ppb Rh) was used to monitor measurement stability. The limiting factor for the precision of the measurements was typically the intensities on the germanium isotopes. Future work could improve the protocol by adapting the Si column protocol to yield higher Si (and thus Ge) concentrations.

Quantification of Germanium Partitioning

Throughout, we enumerate the discrimination of Ge relative to Si through the use of an exchange coefficient, K_D, following the terminology of Beattie and others (1993):

$$K_D = \frac{\left({}^{\mathrm{Ge}}/_{\mathrm{Si}}\right)_{\mathrm{solid}}}{\left({}^{\mathrm{Ge}}/_{\mathrm{Si}}\right)_{\mathrm{solution}}} \quad (1)$$

Importantly, this is an apparent, or bulk exchange coefficient, while a true exchange coefficient for trace-element partitioning depends on the stoichiometry of the mineral forming (Prieto, 2009; Perez-Fodich and Derry, 2020). KD is analogous to an isotope fractionation factor α (Coplen, 2011). Note that in the literature, K_D is variously

termed a distribution coefficient, a partition coefficient, or a fractionation factor (for example, Froelich and others, 1992; Kurtz and others, 2002; Blecker and others, 2007; White and others, 2012).

RESULTS

Ge concentrations and Ge/Si ratios for the reference materials BHVO-2, BIR-1a and Rye Grass agree well with published values (table 2). We also present new results for the reference materials NBS28, Diatomite and Japanese Chert 1 (JCh-1) for future use as Ge/Si reference materials. We also note that the Ge/Si ratios we measure for soils and river waters of the KREW watersheds (see below), including very low river solute ratios, agree well with independently generated data by isotope-dilution hydride-generation ICP-mass spectrometry (Aguirre, ms, 2019). As a conservative estimate of uncertainty on the Ge/Si ratios we use 2 standard deviations of the BHVO-2 measurements ($\pm$ 0.26 μmol mol^{-1}, n = 12), encompassing multiple digestions and analytical sessions. Preliminary analyses show that this precision is improved at higher solution Si concentrations, suggesting the potential for future improvement to the analytical protocol.

A site-wise summary of Ge/Si ratios for bulk soils and saprolite, clay size fractions, plant material, and water samples is given in table 3 and figure 2. Full details of the results, along with silicon isotope ratios (from Frings and others, 2021a) and bulk chemical compositions (from von Blanckenburg and others, 2021) are provided in an open-access online publication hosted at GFZ data services (Frings and others, 2021b) hereafter called 'Data Tables.' The aim is to make this data readily available for global compilations. All samples have been assigned a unique identifier, an 'International Geo-Sample Number' (IGSN). Full sample metadata is linked to IGSNs at http://igsn.org.

Bedrock at all three sites has a similar Ge/Si ratio (1.2 to 1.7 μmol mol^{-1}; table 3). Water samples at all three sites have the lowest Ge/Si ratios, below 1 μmol mol^{-1}, with Ge concentrations in the column elutions often falling below instrumental detection limits, even after partial evaporative enrichment. Bulk soil and saprolite samples have Ge/Si close to bedrock (1.34–3.71 μmol mol^{-1}). Ge/Si ratios in plant samples are variable, including values both below and above parent rock (from <0.10 to 4.42 μmol mol^{-1}). Clay-size fraction samples from all three sites span a range of almost 5 μmol mol^{-1} (from 1.58 to 6.33 μmol mol^{-1}) in their Ge/Si ratio and are systematically higher than bedrock.

The three sites differ in the Ge/Si ratios of the various pools. Stream and water samples from Sri Lanka have the highest values, while those from Sierra Nevada are the lowest (almost uniformly with Ge below detection). Similar tendencies are exhibited in the bulk soil and saprolite samples, and the clay size fractions: Sri Lanka has the highest values, while Sierra Nevada and the Swiss Alps have lower ratios (table 3, fig. 2).

DISCUSSION

Ge and Si Partitioning in the Critical Zone

Our Ge/Si data define trends with the associated silicon isotope distributions (fig. 3; Frings and others, 2021a). During initial weathering, germanium and silicon are solubilized from silicate minerals. We assume that any potential non-stoichiometric release cannot be maintained as the mineral grain progressively dissolves, such that the solute has a ratio that reflects that of the mineral(s) dissolving. As secondary minerals precipitate, they tend to preferentially incorporate Ge over Si, and ^{28}Si over ^{30}Si, in their structures or adsorbed to their surfaces (fig. 3A–C, E). Most of the

TABLE 2

Overview of reference materials measured in this study and compilation of literature Ge concentrations and/or Ge/Si ratios

Reference material	This study				Literature			
	Si concentration (wt %)	Ge concentration (µg g^{-1})	Molar Ge/Si (µmol mol^{-1})	*n*	Si concentration (wt %)	Ge concentration (µg g^{-1})	Molar Ge/Si (µmol mol^{-1})	Reference
NBS28 (NIST RM 8546)	--	--	0.38 ± 0.05	5	--	--	--	--
BHVO-2	--	--	2.72± 0.13	12	*Certified value: 23.19 ± 0.07*	1.47	*2.45*	D19
						1.59	*2.65*	S06
						1.62 ± 0.04	*2.70*	J05
BIR-1	21.74 ± 0.24	1.45 ± 0.042	2.72 ± 0.05	16	*Certified value: 22.34 ± 0.07*	1.52	*2.63*	K02
						1.45	*2.51*	MF87
						1.53	*2.65*	MF96
						1.46	*2.53*	J05
					23.5	1.55	2.55	B18
					21.6	1.55	2.77	B18
Rye Grass (ERM-CD281)	0.20 ± 0.01	0.06 ± 0.001	13.49 ± 1.01	8	0.13	0.07	20.82	D19
Diatomite	--	--	0.66 ± 0.02	4	--	--	--	--
JCh-1	43.89 ± 0.86*	0.71 ± 0.02	0.676 ± 0.015	8	45.72 ± 0.23	--	--	I96

References: B18: Baronas and others (2018), D18: Delvigne and others (2018), I96: Imai and others (1996), J05: Jochum and others (2005), K02: Kurtz, Derry, and Chadwick (2002), MF87: Mortlock and Froelich (1987), MF96 Mortlock and Froelich (1996), S06: Scribner and others (2006). Italicised values indicated literature values for BHVO-2 and BIR-1 Si concentrations taken from GeoRem database and used to calculate Ge/Si ratios. Literature Si concentration for ERM-CD281 from IRMM recommended value (one analysis only). *One outlier rejected.

TABLE 3

Summary of Ge/Si ratios in different ecosystem components in the Alps-Sierra Nevada-Sri Lanka erodosequence

	Bedrock	Bulk soil/saprolite	Clay size fraction	Plant material	Water samples
Alps	1.71 ± 0.04, n = 6*	1.66 ± 0.32, n = 9	2.76 ± 1.13, n = 18	3.10 ± 1.43, n = 10	0.51 ± 0.32, n = 4
Sierra Nevada	1.79 ± 0.14, n = 7*	2.22 ± 0.22, n = 12	3.91 ± 0.64, n = 23	2.00 ± 1.16, n = 6	<0.10, n = 6
Sri Lanka	1.23 ± 0.03, n = 4	2.29 ± 0.63, n = 15	4.89 ± 0.92, n = 25	2.42 ± 1.21, n = 6	0.46 ± 0.14, n = 4

A full breakdown is given in the supporting Data Tables hosted at GFZ data services (Frings and others, 2021b).
* 1 outlier removed.

solubilized Ge thus ends up in the high-Ge/Si clay size fraction, and only a small fraction is exported from the system as dissolved Ge. River waters thus have lower Ge/Si ratios and higher δ^{30}Si (fig. 2; fig. 3A–C), an observation that is consistent across tropical, subtropical, and arctic systems (Kurtz and others, 2002; Anders and others, 2003; Lugolobi and others, 2010; Ameijeiras-Mariño and others, 2018; Baronas and others, 2018, 2020). Bulk soils and saprolites represent a balance between moderate Ge/Si primary minerals, and high Ge/Si secondary minerals (Ameijeiras-Mariño and others, 2018), and so tend towards higher values along the weathering intensity gradient Alps-Sierra Nevada-Sri Lanka (fig. 3A–C, D) as secondary minerals become a proportionally larger component of the soil.

Interpreting river solute Ge/Si ratios can be non-trivial, since they reflect a balance of all Critical Zone processes and thus time-dependent contributions from various solute sources (for example, Kurtz and others, 2012; Ameijeiras-Mariño and others, 2018). Additionally, at least four non-weathering controls on stream water Ge/Si ratios have been documented. First, settings experiencing fly-ash deposition from the burning of coal with high Ge concentrations (Froelich and others, 1985). Second, systems with localised hot-spring or other hydrothermal inputs that can introduce waters with Ge/Si ratios up to 1000 μmol mol^{-1} (Evans and Derry, 2002). Third, systems where a large fraction of the solute flux is generated subglacially tend to have elevated Ge/Si ratios (Anders and others, 2003), suggested to reflect the preferential dissolution of high Ge/Si biotite (typically $>$ 5 μmol mol^{-1}). Fourth, in-stream production of diatom biomass with an associated discrimination against either Si or Ge may shift riverine Ge/Si. There is no evidence for extensive pollution or hydrothermal activity in these sites, and none are glaciated. Stream lengths are short, and most biogenic silica is likely terrestrial rather than aquatic (Cary and others 2005, Schoelynck and others 2019). We thus assume all measured ratios can be interpreted in terms of Critical Zone biogeochemical processes.

A factor that we lack the data to fully evaluate is the importance of inter-mineral heterogeneity in Ge/Si. Elsewhere, it is shown that Si isotope ratios differ by up to 0.85 ‰ among minerals (Frings and others, 2021a), so incongruent dissolution at the rock scale might induce variation in the δ^{30}Si of Si released during solubilisation. We do not have mineral-specific Ge/Si ratios for the rocks underlying the Alps, Sierra Nevada and Sri Lanka, but the available evidence suggests they may differ substantially. Since at least 1943, it has been realised Ge preferentially substitutes for Si in the least-linked tetrahedra (Wickman, 1943). Early work (Novokahatskiy and others, 1967, cited in Mortlock and Froelich, 1987) yielded biotite values of *ca.* 9 μmol/mol and quartz ratios of $<$ 1 μmol mol^{-1}, in line with the Wickman (1943) rule. This

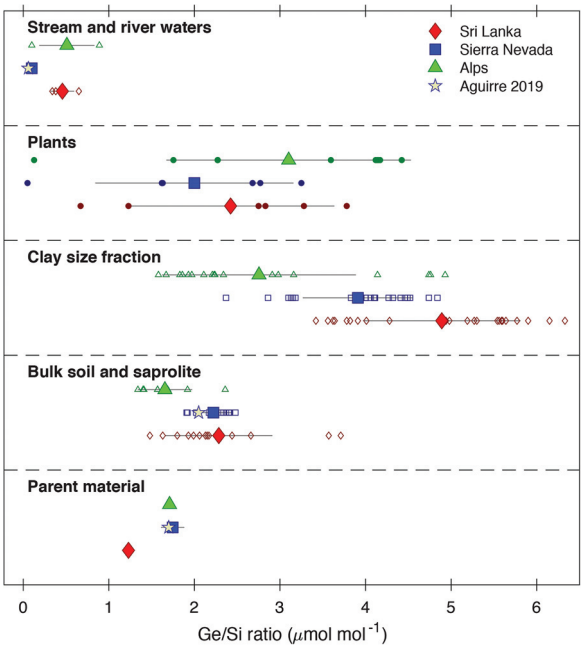

Figure 2. Summary of Ge/Si ratios in different CZ compartments in the Alps-Sierra Nevada-Sri Lanka erodosequence. Large filled symbols with bars represent site-averages ±1σ, small open symbols represent individual samples. Also shown as open symbols is independently generated data from Aguirre (ms, 2019) for waters, bulk soils, and parent rock of the same Sierra Nevada site. The data show the general partitioning of material solubilized from rock into high Ge/Si secondary phases and plants and low Ge/Si river solutes.

observation has been repeated many times since. Biotite, from a diverse range of settings, is consistently high Ge/Si: 4 μmol mol^{-1} in Himalaya gneisses (Evans and Derry, 2002), 4.1 μmol mol^{-1} in a biotite–muscovite gneiss in southern California (Filippelli and others, 2000); 5.2 to 6.1 μmol mol^{-1} in a Puerto Rican granodiorite (Kurtz and others, 2002, Lugolobi and others, 2010). Aguirre and others (2017) measured biotite Ge/Si of 2.58 in a Colorado gneiss, but flagged potential quartz inclusions. Most other rock-forming minerals have consistently lower Ge/Si: plagioclase, muscovite and kyanite in the Himalayan gneiss are around 2 μmol mol^{-1}, muscovite in the Californian gneiss is 2.0 μmol mol^{-1}, and quartz in the Puerto Rico diorite is 0.5 μmol mol^{-1}. Feldspar in the Puerto Rico diorite is also lower Ge/Si, at around 1.5 μmol mol^{-1} (Lugolobi and others, 2010). Here, we assume that the Ge/Si ratio of solubilized Si is equivalent to bulk rock but acknowledge that future work could test the validity of this assumption via *in situ* analytical techniques or digestion of mineral separates.

Germanium Discrimination During Plant Uptake?

Our data is inconsistent with the assumption that both plants and clays partition Ge relative to Si in opposite directions. The current paradigm is that plants ostensibly discriminate against Ge and thus have lower Ge/Si ratios than bedrock (Kurtz and Derry, 2004; Derry and others, 2005; Blecker and others, 2007; Delvigne and others, 2009; Cornelis and others, 2010; Lugolobi and others, 2010; White and others, 2012; Meek and others, 2016). However, plant material analysed in this study does not show the expected discrimination of Ge over Si during plant uptake. Indeed, with only a

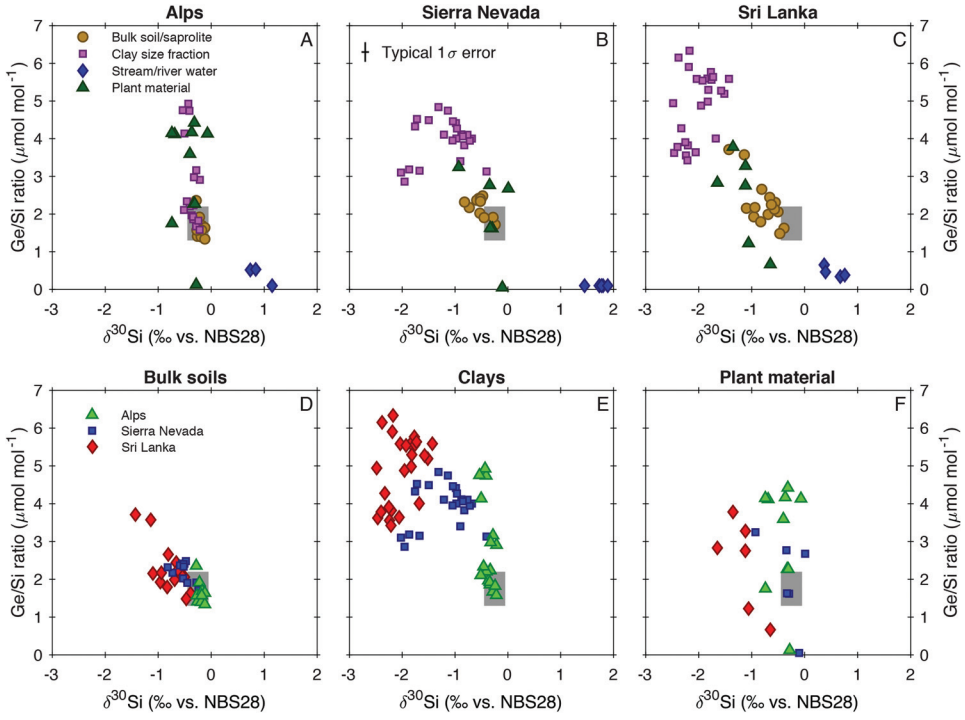

Figure 3. A comparison between Ge/Si ratios and $\delta^{30}Si$ (Frings and others, 2021a), two geochemical tracers of silicon partitioning at the Earth's surface. Panels A-C show different CZ compartments at each of the sites in the Alps-Sierra Nevada-Sri Lanka erodosequence. Panels D-F show data from all three of the sites separated into bulk soil/saprolite, the clay size fraction, and plant material. The grey shaded area is an approximation of typical granitoid bedrock values.

few exceptions the plant samples have Ge/Si ratios in the range of parent material or higher (fig. 3F). Assuming that stream water is a good approximation of the soil water the plants obtain their Si from, we can calculate K_D^{veg} values of *ca.* 5 (Alps and Sri Lanka) to >20 (Sierra Nevada) (see table A1).

One key difference between our analytical protocol and those previously published is the pre-treatment of plant material prior to dissolution. Essentially, most previous work reports Ge/Si ratios of phytolith extracts (Kurtz and Derry, 2004; Derry and others, 2005; Blecker and others, 2007; Delvigne and others, 2009; Cornelis and others, 2010; Lugolobi and others, 2010, White and others, 2012; Meek and others, 2016). In contrast, the bulk plant analysis by NaOH fusion performed here targets phytolith silica plus any non-phytolith plant silicon pools. Table A1 summarises the range of phytolith Ge/Si and K_D^{veg} (eq 1) values observed in previous experimental and empirical work. Two related observations stand out. First, experiments that track the evolution of Ge and Si in hydroponic growth solutions suggest no resolvable discrimination of Ge relative to Si during plant uptake (Rains and others, 2006; Delvigne and others, 2009). Conversely, measurements of phytolith Ge/Si ratios require discrimination at some stage before phytolith precipitation. Second, when analysed separately, root material often has higher Ge/Si than stem or leaf material (Delvigne and others, 2009).

Two non-exclusive explanations for the hydroponics/phytolith discrepancy exist: preferential Ge sequestration relative to Si in plant roots, or a high Ge/Si plant Si pool that is not sampled by the phytolith extraction protocols. In support of the

hypothesis of preferential Ge sequestration in roots, Ge/Si ratios in the roots of Banana (*Musa acuminata*) and Horsetail (*Equisetum* sp.) grown in natural soils have been shown to be high (> 2.3 μmol mol^{-1}) in some settings (Delvigne and others, 2009), though not in Western Wheatgrass (*Agropyron smithii*) (Blecker and others, 2007). It is also supported by the demonstration of low Ge/Si ratios (< 0.6 μmol mol^{-1}) in sap waters of three temperate tree species (Meek and others, 2016), suggesting that discrimination against Ge relative to Si occurs somewhere during or before transport across the root endodermal cell layer into the vascular system. *In situ* imaging of the roots and shoots of grasses by secondary ion mass spectrometry demonstrated that Si and Ge are highly localised and not equally distributed (Sparks and others, 2011) – the ratio of Ge to Si was greater in roots than shoots of blue grass (*Poa annua*) and orchard grass (*Dactylis glomerata*). Again, this suggests the preferential transport of Si relative to Ge through the xylem. Arguing against preferential root Ge sequestration as the sole explanation, the Ge/Si ratios measured in the dominant species of plants along the Alps-Sierra Nevada-Sri Lanka erodosequence (from 0–4.4 μmol mol^{-1}, table 3 and fig. 3F) require that at least in some taxa, Ge is preferentially transported through the xylem. Yet it is apparently not found in phytoliths (table A1). This requires a non-phytolith, high Ge/Si pool in vascular plants.

In support of the suggestion of a Ge-rich and non-phytolith Si pool, analyses of whole plant samples following a lithium-borate fusion by Delvigne and others (2009) and Delvigne and others (2018) corroborate the observation of high Ge/Si ratios in bulk plant biomass. The nature of this pool is unclear. Since Ge is more readily complexed by organic molecules than Si (Pokrovski and Schott, 1998), one possibility is that Ge but not Si is hosted in organic compounds, perhaps sulphur-containing proteins (Wiche and others, 2018). Alternatively, plant bio-silica deposits besides micrometre size phytoliths could have high Ge/Si ratios. Multiple high-resolution spectroscopic and microscopic studies of plant Si localisation allow plant silica precipitation to be classified into three pathways: silica deposition onto carbohydrate matrices, silica deposition in the cell lumen without an obvious matrix; and in intercellular spaces (Sangster and others, 2001; Hodson, 2016, 2019), with distinct chemistries, morphologies and structures. The first two pathways produce distinctive phytoliths that can persist in the soil following leaf abscission and decomposition (Strömberg and others, 2016). The last pathway apparently produces fragile smaller silica bodies (Sommer and others, 2006). Because these different forms of plant silica are precipitated via different mechanisms, it is plausible they have variable Ge/Si ratios. Thus, Ge may be found in leaves either associated with reactive Si phases, or in organic compounds, that are solubilized by acid and/or oxidative leaching steps in phytolith extraction protocols.

To our knowledge, the only determinations of Ge/Si ratios in an acid leaching step before phytolith dissolution have recently been published by Kaiser and others (2020). They observe that in three graminoid species, the majority (>80 %) of Ge is contained in a non-phytolith pool. In contrast, phytoliths comprise the majority of the plant Si pool (> 70 %) but have Ge/Si ratios a factor of 10 lower. *In situ* analysis by laser-ablation ICP-MS confirmed that Ge is distributed throughout leaf cells, while Si is localised in phytoliths (Kaiser and others, 2020). Our data adds support from field settings to these experimental results and questions the paradigm that plants and secondary clays have differential discrimination of Ge relative to Si.

The concept of two discrete plant pools with different Ge/Si ratios creates the potential for differential recycling efficiencies. Mass balance models of the style proposed by Bouchez and others (2013), that we explore in more detail below, assume that eroding organic matter is equivalent in composition to living biomass. If the putative Ge-rich organic phase remineralises more quickly than the Ge-poor phytolith

phase, for example, then this assumption may not hold. On the other hand, the Ge-rich phase might be more susceptible to erosion, or even subsurface transport (Kim, Gu, and Brantley, 2018). We can begin to explore the sensitivity of models to these issues (see section 'Application of Coupled Ge/Si-δ^{30}Si Mass Balance Models'), but ultimately future work could seek to experimentally determine the labilities and erosive susceptiblites of the two Ge-containing plant pools.

The heterogeneity in our measured plant sample Ge/Si ratios may be related to the plant species, which in turn may be related to the presence of specific Si transporters and dominant form of silicification. Wiche and others (2018) review the genetic and physiological basis of plant Ge uptake, concluding that species is an important control on Ge uptake kinetics, and thus presumably Ge/Si discrimination. The highest plant Ge/Si ratios we measure (>4 μmol mol^{-1}) derive from moss samples in the Alps. While the emergence of biosilicification mechanisms among landplants is a complex and poorly understood subject (Trembath-Reichert and others, 2015), mosses have some of the earliest diverging proteins that constitute the aquaporins (transmembrane proteins) responsible for dissolved Si uptake. Thus, it is reasonable that they have subtly different Ge uptake and deposition mechanisms. Overall, any intra-species differences in bulk Ge/Si ratios are deserving of further investigation.

Germanium Partitioning into Secondary Weathering Products

Any quantitative interpretation of Ge/Si ratios in river water or clays requires the discrimination of Ge relative to Si into clays to be known. The preferential incorporation of one element over another into a phase is enumerated by an exchange coefficient K_D^{sec} (eq 1). The available data consistently suggest Ge is preferentially incorporated. These estimates include K_D^{sec} = 1.6 for the synthesis of allophane ($Al_2O_3(SiO_2)_2$) at 90 °C (Kurtz and others, 2002), and $K_D^{sec} \approx 3$ for the formation of kaolinite from plagioclase in Puerto Rico (Kurtz and Derry, 2004, Scribner and others, 2006). Cornelis and others (2010) report clay size fraction Ge/Si ratios of 6.1 and 6.3 μmol mol^{-1} for two samples from a beech forest in central France. XRD revealed these were a mixture of quartz, kaolinite, illite, illite–vermiculite mixed layers, smectite, and chlorite. Corresponding soil solutions had a Ge/Si ratio of 1.4 μmol mol^{-1}, producing $K_D^{sec} \approx 4.4$. Elsewhere, Aguirre and others (2017) present Ge/Si data for the clay-size fraction from borehole soil samples from a small Colorado catchment underlain by biotite gneiss. These average 2.47 μmol mol^{-1} (n = 3), but a geochemical correction to account for quartz results in a kaolinite Ge/Si of 5.2 μmol mol^{-1}. Groundwater Ge/Si ratios varied between 0.2 to 0.5 μmol mol^{-1}, depending on sampling site, yielding K_D^{sec} = 10.4 to 26. Finally, four clay samples from intensely weathered soils developed over andesitic lava flows in Costa Rica averaged 7.35 μmol mol^{-1} (Baronas and others, 2020). Local streams and groundwater seeps (n = 15) were lower Ge/Si (mean = 0.60), producing a face-value estimate of K_D^{sec} of 12.3. The authors use a more sophisticated approach based on local soil-water chemistry and the mass-balance model in Baronas and others (2018) to derive K_D^{sec} = 3.4: still a substantial positive discrimination of Ge relative to Si.

Two novel approaches also permit estimates of K_D^{sec} associated with clay formation. First, in a range of global rivers, an inversion of a germanium and silicon isotope mass-balance model yielded K_D^{sec} from 2 to 22 (Baronas and others, 2018, Baronas and others, 2020). A conceptually similar reactive-transport-model applied to groundwater flowing through volcanic tuff in Costa Rica suggested K_D^{sec} = 10 (Baronas and others, 2020). Second, Perez-Fodich and Derry (2020) take a thermodynamic approach to determine K_D^{sec} for kaolinite, in a approach that is independent of field data. They

derive a best-estimate of 50 (range: 9–280), in good agreement with the experimental, soil-profile and catchment scale studies reviewed above.

Preferential incorporation of Ge into secondary weathering products also finds qualitative support elsewhere. Opfergelt and others (2010) present Ge/Si ratios for the clay size fraction of basaltic soils in Cameroon that average 4.28 ± 1.05 μmol mol^{-1} (mean ± 1σ, $n = 18$) – above local bedrock (2.21 μmol mol^{-1}), but with no corresponding dissolved load data. Anders and others (2003) present experimental data showing that Ge is preferentially adsorbed relative to Si on to hydrous iron oxides, but do not quantify a partition coefficient. Pokrovsky and others (2006) performed adsorption experiments of Ge onto goethite. By comparison of their results with other experimental studies focusing on silicon (for ecample, Dietzel, 2002), they conclude Ge is preferentially adsorbed. In their pioneering work, Murnane and Stallard (1990) quantify Ge/Si exchange coefficients of 1.3 to 2.7 but consider only bulk solid material rather than any specific mineral phase. Overall, all available data thus suggests that formation of secondary minerals is associated with $K_D^{sec} > 1$, that is, Ge is preferentially partitioned into secondary silicate phases or adsorbed onto oxide surfaces, relative to Si.

The dominant clay mineral forming in the Sri Lanka site is kaolinite (Behrens and others, 2015). XRD analysis of bulk samples from the Sierra Nevada sites detected only kaolinite (Uhlig and others, 2017), although analysis of clay size separates – which should be more sensitive – from a nearby site also identified hydroxyl-Al interlayered vermiculite and gibbsite (Dahlgren and others, 1997). No XRD analysis has been undertaken on the Swiss Alps samples. However, the clays in soils forming nearby under similar climate and on similar parent lithology (Drever and Zobrist, 1992, Egli and others, 2001) are dominated by primary phyllosilicates (chlorites and micas) or the incipient/early products of weathering (a 'hydrobiotite'), plus limited smectite and kaolinite. Note that unlike Frings and others (2021a), but in line with previous work, we do not account for the potential 'contamination' of the clay size fraction by primary minerals, since their Ge concentrations are not well-constrained. In Sri Lanka, the average clay size fraction has a Ge/Si ratio of 4.89 μmol mol^{-1}. In Sierra Nevada, this ratio is 3.91 μmol mol^{-1} and in the Alps it is 2.76 μmol mol^{-1} (table 3). Measured dissolved ratios take values of 0.46 and 0.51 μmol mol^{-1} for Sri Lanka and the Alps, respectively. Our Sierra Nevada stream water ratios (<0.1 μmol mol^{-1}); samples from 2010–2014) are in strikingly good agreement with the 2009 water year data from the same catchments measured by hydride-generation isotope-dilution ICP-MS by Aguirre (ms, 2019) (mean ± 1σ Ge/Si = 0.06 ±0.02 μmol mol^{-1}, $n = 39$). These ratios produce K_D^{sec} of 10.7 in Sri Lanka, 65 in Sierra Nevada, and 5.4 in the Alps. Independently generated soil water Ge/Si ratios from the same Providence Creek catchments in Sierra Nevada are higher (1.19±0.53 μmol mol^{-1}, $n = 26$; Aguirre (ms, 2019)) and yield $K_D^{sec} = 3.29$. The K_D^{sec} values derived from stream-water Ge/Si thus do not necessarily reflect the sub-micrometre scale process of clay formation, but rather the net result of all catchment processes, in a similar way to the isotope fractionations in the mass-balance model of Bouchez and others (2013).

The calculated K_D^{sec} values for the erodosequence sites and the available literature data are not clearly linked to weathering intensity or secondary-phase mineralogy. A mechanistic explanation for the range of K_D^{sec} requires further work but may lie in the different aqueous behaviour of Ge and Si. In particular, as discussed above Ge is more likely to form stable complexes with functional groups in common soil organic acids (Pokrovski and Schott, 1998). Future work could focus on understanding the wide range of observed K_D^{sec} values for the Ge/Si system.

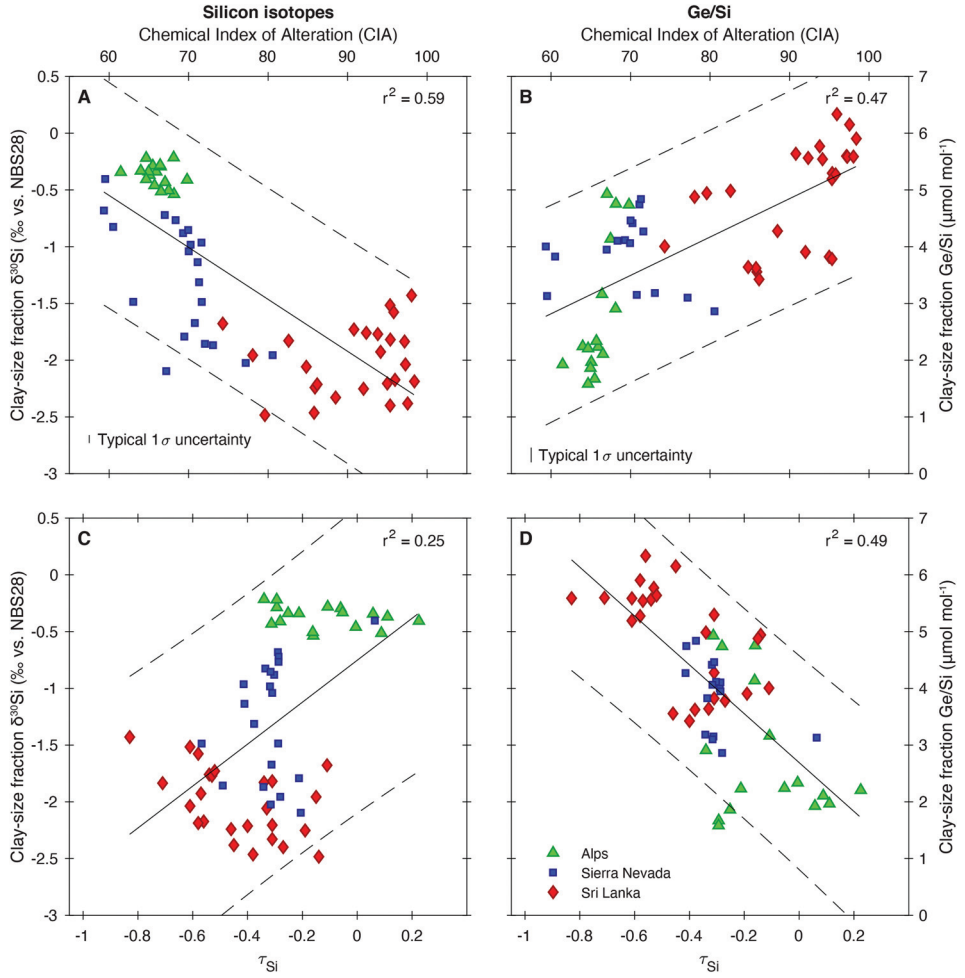

Figure 4. Comparison of the utility silicon isotope ratios (A, C) and Ge/Si ratios (B,D) in clay size fractions as proxies for weathering intensity. Both are plotted against two indices of bulk soil/saprolite weathering progression: the Chemical Index of Alteration (CIA; panels A,B; eq 2 in main text) or τ_{Si} (panels C,D; eq 3 in main text). Solid lines depict least-squares linear regressions through the data, with the amount of variance in δ^{30}Si or Ge/Si explained by the CIA or τ_{Si} given in the upper right. Dashed lines represent 95 % confidence intervals on the regressions. The results show that Ge/Si is equally powerful as a weathering intensity proxy as silicon isotope ratios.

Ge/Si Ratios as a Weathering Proxy

A compilation of bulk soil silicon isotope ratios from soils shows that δ^{30}Si values decrease with increasing weathering intensity, defined as the fraction of total denudation that is accomplished chemically (Opfergelt and Delmelle, 2012; Frings and others, 2021a). Along a land-use gradient on rhyodacitic soils, Ameijeiras-Mariño and others (2018) demonstrate that the same concept applies to Ge/Si ratios of bulk soil. Frings and others (2021b) and Bayon and others (2018) also demonstrate that the clay size fraction δ^{30}Si itself is a sensitive tracer of weathering. This gives clays utility as a potential (palaeo)weathering proxy, since the clay size fraction is presumably minimally biased by size and density sorting during transport and deposition (Dinis and others, 2019).

In figure 4, we show both δ^{30}Si and Ge/Si ratios of the clay size fraction as a function of two widely used weathering indices: the chemical index of alteration (CIA; Nesbitt and Young, 1982) and the Si mass-transfer coefficient τ_{Si} (Brimhall and Dietrich, 1987). The CIA is calculated from the concentrations (in wt%) of major oxides:

$$\mathrm{CIA} = \left[\frac{\mathrm{Al_2O_3}}{\mathrm{Al_2O_3} + \mathrm{CaO^*} + \mathrm{Na_2O} + \mathrm{K_2O}}\right] \cdot 100 \tag{2}$$

where $\mathrm{CaO^*}$ refers to the calcium content of silicate minerals only. CIA does not consider parent composition, but typically takes a value of around 50 for unweathered granites and granodiorites and increases to a maximum of 100 with the progressive loss of the cations Ca^{2+}, Na^+ and K^+. The mass-transfer coefficient τ_{Si} is defined as:

$$\tau_{Si} = \frac{[\mathrm{Si}]_{\mathrm{soil}}}{[\mathrm{Si}]_{\mathrm{rock}}} \times \frac{[\mathrm{Zr}]_{\mathrm{rock}}}{[\mathrm{Zr}]_{\mathrm{soil}}} - 1 \tag{3}$$

where the subscripts rock and soil refer to concentrations in the parent rock and the weathered soil/regolith material, respectively, and where Zr is assumed immobile during weathering. A τ_{Si} value of 0 implies no loss of Si, while τ_{Si} of *ca.* −0.5 denotes the maximum Si loss typically attainable in felsic rock (given the presence of quartz).

Empirically, Ge/Si ratios in clays are at least as useful as silicon isotopes as a weathering proxy: the same strength correlation exists between the weathering indices CIA and τ_{Si}, and the δ^{30}Si values and Ge/Si ratios of the clay fractions (fig. 4), corroborating the results of Baronas and others (2020). Samples from Sri Lanka have the highest weathering intensity, the lowest δ^{30}Si values and the highest clay Ge/Si. Samples from the Alps show the lowest weathering intensity, the highest δ^{30}Si values and the lowest clay Ge/Si. Sierra Nevada takes intermediate values. Hence, both Si isotope ratios and Ge/Si ratios of the clay size fraction can be used as tracers for the weathering intensity of bulk soil and saprolite samples, even in the absence of parent material for indexing weathering degree to (see also Baronas and others, 2020). Since the determination of Ge/Si ratios is analytically simpler than δ^{30}Si, Ge/Si ratios in clays have promise as a widely applicable silicate weathering proxy.

Application of Coupled Ge/Si-δ^{30}Si Mass Balance Models

To explore how Ge/Si evolves between secondary solids and solutes we employ a mass-balance framework. For stable isotope ratios, a well-established mass-balance tracks the evolution of isotope ratios (in "δ" notation) in the dissolved pool as a function of (i) the partitioning f of the export flux of that element between a fractionated solid product and a residual dissolved phase, and (ii) the fractionation ε associated with that partitioning:

$$\delta_{residual} = \delta_{initial} - \varepsilon(1 - f) \tag{4}$$

$$\delta_{product} = \delta_{initial} - \varepsilon f \tag{5}$$

As noted elsewhere (for example, Criss, 1999, Hayes, 2004), these are approximations of more rigorous calculations of isotope ratios that suffice because ε is typically very small (that is, a few per mil). Working with ratios (rather than δ-values) allows these

frameworks to be extended to trace-major element ratios. For the example of the germanium-silicon 'pseudoisotope' ratio as fractionated solids form from a solution:

$$K_D^{sec} = \frac{\left(\mathrm{Ge}/\mathrm{Si}\right)_{\mathrm{solid}}}{\left(\mathrm{Ge}/\mathrm{Si}\right)_{diss}} = \frac{f_{solid}^{Ge} * \ Ge_{tot}}{f_{solid}^{Si} * \ Si_{tot}} / \frac{f_{diss}^{Ge} * \ Ge_{tot}}{f_{diss}^{Si} * \ Si_{tot}} \tag{6}$$

where the subscripts 'solid', 'diss' and 'tot' denote the fractionated secondary solids, dissolved material, and bulk system, respectively, and f is the fraction of Ge or Si in either phase. Since $f_{solid}^{X} + f_{diss}^{X} = 1$, equation (6) can be expressed as:

$$K_D = \frac{f_{solid}^{Ge} \cdot \left(1 - f_{solid}^{Si}\right)}{f_{solid}^{Si} \cdot \left(1 - \ f_{solid}^{Ge}\right)} \tag{7}$$

Solving for f_{solid}^{Ge}:

$$f_{solid}^{Ge} = \frac{K_D * \ f_{solid}^{Si}}{1 + f_{solid}^{Si}(K_D - 1)} \tag{8}$$

Since $(Ge/Si)_{solid}$ is the numerator of the terms in equation (6) (that is, $(Ge/Si)_{solid} = \left(f_{solid}^{Ge}/f_{solid}^{Si}\right) \cdot (Ge/Si)_{tot}$, and assuming that the Ge/Si ratio of the total system ($(Ge/Si)_{tot}$) is equivalent to that of parent material (that is, congruent dissolution), then simplifying yields an expression for the Ge/Si ratio of fractionated secondary phase as a function of Si partitioning into secondary solids (that is, f_{solid}^{Si}) and parent composition:

$$\left(\mathrm{Ge}/\mathrm{Si}\right)_{\mathrm{solid}} = \frac{K_D\left(\mathrm{Ge}/\mathrm{Si}\right)_{parent}}{1 + \ f_{solid}^{Si} \ (K_D - 1)} \tag{9}$$

And $(Ge/Si)_{diss}$ is thus similarly:

$$\left(\mathrm{Ge}/\mathrm{Si}\right)_{\mathrm{diss}} = \frac{\left(\mathrm{Ge}/\mathrm{Si}\right)_{\mathrm{parent}}}{1 + \ f_{solid}^{Si} \ (K_D - 1)} \tag{10}$$

Figure 5 shows these relationships graphically. These expressions can also be applied to isotope ratios, with K_D becoming the fractionation factor (expressed as α) and the raw isotope ratio (that is, not expressed in delta-notation) replacing Ge/Si. This framework is conceptually similar to the two-endmember mixing model for Ge/Si ratios in stream water (for example, Froelich and others, 1992; Kurtz and others, 2002). For the possible range of f_{solid}^{Si} (that is, 0 to 1), Ge/Si ratios predicted for the secondary solids fall between $(\mathrm{Ge}/\mathrm{Si})_{\mathrm{parent}}$ and $K_D(\mathrm{Ge}/\mathrm{Si})_{\mathrm{parent}}$. For dissolved Si and Ge, the range is $K_D(\mathrm{Ge}/\mathrm{Si})_{\mathrm{parent}}$ to $(\mathrm{Ge}/\mathrm{Si})_{\mathrm{parent}}$. Since K_D between secondary clays and dissolved loads is > 1 (section 'Germanium Partitioning Into Secondary Weathering Products' above), this demonstrates why Ge/Si ratios in secondary solids should be more sensitive as a weathering proxy than solutes. For a given analytical uncertainty on Ge/Si ratios the resolvable change in secondary mineral vs. dissolved load Si partitioning (the x-axis in fig. 5) is smaller for ratios from secondary clays than solutes. Indeed, figure 4 shows how Ge/Si ratios in clay fractions correlate well with indices of weathering intensity along the erodosequence. Conversely, Ge/Si ratios in

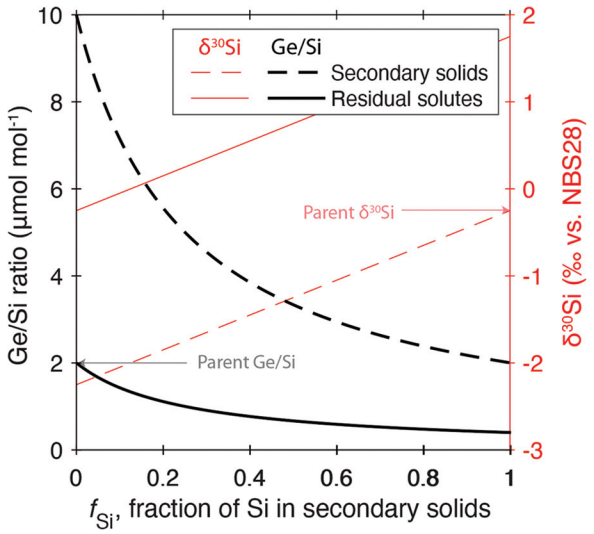

Figure 5. Evolution of Ge/Si ratios in fractionated secondary solids and residual dissolved Si and Ge, as a function of the fraction of dissolved Si partitioned into secondary solids (f^{Si}_{solid}), based on equation (9) and equation (10). This example uses a solution initial Ge/Si ratio of 2 µmol mol^{-1} and K_D = 5. Also shown in red is the evolution of silicon isotope ratios in the same material as a function of f^{Si}_{solid} and a fractionation factor α calculated using the same equations but rescaled to the more conventional δ^{30}Si notation for plotting. These lines depict a scenario with an initial solution composition of −0.25 ‰ and a fractionation factor of 0.998. These lines appear straight because α is very close to unity. The error introduced on δ^{30}Si using the approximations of equation (4) and equation (5) instead of equation (9) and equation (10) is less than 0.005 ‰. This figure shows that we would expect Ge/Si ratios of secondary phases to be a more sensitive tracer of weathering congruency (that is, f^{Si}_{solid}) than Ge/Si ratios in stream water.

stream waters at the most (Sri Lanka) and least (Alps) intensely weathered sites overlap (fig. 2). Thus, although Ge/Si ratios in river waters were among the first geochemical weathering intensity proxies (for example, Murnane and Stallard, 1990), Ge/Si ratios of secondary minerals appear to be a more sensitive weathering proxy.

Figure 5 also permits a comparison of Ge/Si ratios and δ^{30}Si for discriminating solid-solute Si partitioning. The ratio of analytical reproducibility (*ca.* 0.25 µmol mol^{-1} and 0.15 ‰) to total signal range is similar for the two proxies, but the form of the expressions in equation (5) and equation (9) means they have different sensitivities at either end of the f^{Si}_{solid} spectrum. At low f^{Si}_{solid}, where most Si is in the dissolved phase, Ge/Si should be a more sensitive proxy than δ^{30}Si. At the other end of the f^{Si}_{solid} spectrum, the Ge/Si curve is flattened and δ^{30}Si should be a more sensitive proxy. This can serve to guide proxy selection for systems where f^{Si}_{solid} can be estimated beforehand, though a combination of both Ge/Si and δ^{30}Si would be most powerful. Building on the work of Baronas and others (2018, 2020), we show below that a strength of a combination of Ge/Si and δ^{30}Si lies in their ability to disentangle the various fluxes that together make up the fractionated solid export.

Quantifying Si Export by River Solutes and in Eroded Clays and Biomass

As applied to a weathering zone, the term f^{Si}_{solid} in equation (9) and equation (10) reflects the balance between export of Si in all fractionated solids and solutes. However, the solids typically comprise many individual components (for Si, particularly secondary minerals and plant biomass). After Bouchez and others (2013), mass-balance equations can be written for any given element in a weathering zone at

steady-state. At steady state, the total element specific denudation rate (t km^{-2} yr^{-1}) is equal to that leaving the zone and is partitioned into a fraction that is solubilized and a fraction that is not:

$$D[X]_{rock} = S_{prim}[X]_{rock} + E_{prim}[X]_{rock} \quad (11)$$

where [X] is the concentration of the element of interest (g g^{-1}), D is denudation (t km^{-2} yr^{-1}), S_{prim} is the rock solubilisation flux (dissolution; t km^{-2} yr^{-1}) and E_{prim} is the physical erosion of unaltered rock (t km^{-2} yr^{-1}). This formulation assumes congruent dissolution at the rock-scale. The fraction of element that is solubilized has three fates:

$$S[X]_{rock} = E_{sec}[X]_{sec} + E_{org}[X]_{org} + W[X]_{TDS} \quad (12)$$

Where E_{clay}, E_{org} and W represent these options: to be eroded as secondary minerals or as biogenic material, or to be removed as solute ('weathered'), respectively (all in t km^{-2} yr^{-1}), and where the subscripts 'sec, 'org', and 'TDS' refer to the element concentration in the pool of clay, biomass, or solute, that is removed. We use the subscript 'org' to denote all plant material, but note that it need not be organic from a molecular perspective. Note that $[X]_{TDS}$ is not a concentration per unit of water, but rather a concentration normalised by the sum of all solutes. Applying this framework to Ge and Si, and normalising by the solubilisation of Ge or Si S results in two mass balance equations:

$$[Ge]_{rock} = e_{clay}[Ge]_{clay} + e_{org}[Ge]_{org} + w[Ge]_{TDS} \quad (13)$$

$$[Si]_{rock} = e_{clay}[Si]_{clay} + e_{org}[Si]_{org} + w[Si]_{TDS} \quad (14)$$

where the lower-case letters denote fluxes normalised to elemental solubilisation. Combining equation (13) and equation (14) results in the mixing equation:

$$\left(\frac{Ge}{Si}\right)_{rock} = e_{sec}^{Si}\left(\frac{Ge}{Si}\right)_{sec} + e_{org}^{Si}\left(\frac{Ge}{Si}\right)_{org} + w^{Si}\left(\frac{Ge}{Si}\right)_{TDS} \quad (15)$$

where the superscripted Si terms denote the proportion of Si in each flux. We can write a similar mixing equation for Si isotopes:

$$\delta^{30}Si_{rock} = e_{sec}^{Si}\delta^{30}Si_{sec} + e_{org}^{Si}\delta^{30}Si_{org} + w^{Si}\delta^{30}Si_{TDS} \quad (16)$$

Including the mass-balance constraint for the solubilized fraction of Si:

$$e_{sec}^{Si} + e_{org}^{Si} + w^{Si} = 1 \quad (17)$$

results in a system of three equations with three unknowns (that is, e_{sec}^{Si}, e_{org}^{Si}, w^{Si}). We solve equations (15), (16), and (17), accounting for uncertainty in the measured silicon isotope and Ge/Si ratios by a Monte Carlo approach to parameter selection (10^6 ensembles with each parameter drawn randomly from a normal distribution with mean and standard deviation as defined in table 3 for Ge/Si. $\delta^{30}Si$ values are given in the supporting Data Tables and summarized in Frings and others (2021a). The low Ge/Si Sierra Nevada water samples are included as a uniform distribution between 0 and 0.1. Figure 6 and table 4 display the results, which imply substantial differences in the way Si is exported at the three sites.

At the long residence time Sri Lanka site, the median fraction of solubilized Si that is exported as solid is 0.32, with 95 % of solutions falling between 0.13 and 0.54 (that is, $\left(E_{org}^{Si} + E_{sec}^{Si}\right)/S_{prim}^{Si} = 0.32^{+0.22}_{-0.20}$). In Sierra Nevada, the same value is $0.75^{+0.24}_{-0.36}$ and in the Alps it is $0.80^{+0.15}_{-0.24}$. The median fraction of solubilized Si that leaves the system as solute (that is, w^{Si}) is 0.68, 0.25 and 0.20 in Sri Lanka, Sierra Nevada, and the Alps, respectively (fig. 6D). Since the plausible solution space resulting from the Monte Carlo analysis largely falls on contours of w^{Si} (lines of constant $e_{sec}^{Si} + e_{org}^{Si}$, with a gradient of −1; see inset panel in fig. 6C), albeit different between the sites, the calculated w^{Si} terms are robust to the uncertainty on measured Ge/Si and Si isotope ratios. This presumably reflects the same direction of isotope-fractionation and element partitioning into clays and biomass. A sensitivity analysis is included in Appendix B, and demonstrates these conclusions are robust to the presence of plausible biases on the input Ge/Si and δ^{30}Si data. An alternative Si isotope only mass-balance approach is given in Appendix C that yields corroborating results.

The first-order conclusion that emerges from this analysis is that fractionated solid export increases with decreasing regolith residence time. We suggest that this can be explained by three factors. First, secondary phases are produced *in situ* relatively quickly as a net part of typical weathering reactions but are at the thermodynamic limit making them resistant to dissolution (Winnick and Maher, 2018). Second, the net weathering reactions at low-weathering intensity sites tend to form smectite-group or similar clays, so a large fraction of solubilized Si is retained in the new solid (Frings and others, 2021a). Finally, plant biosiliceous production effectively takes subsurface soil water dissolved Si and returns it to the soil surface in an easily erodible form. These factors combine to mean a larger proportion of the solubilized Si is exported as a fractionated solid in the Alps and Sierra Nevada, than in Sri Lanka. Note also that this is equivalent to the section of the hyperbola extending from the maximum to its right hand side that emerges from a plot of dissolved δ^{30}Si or δ^{7}Li against weathering intensity (W/D, the fraction of total denudation accomplished chemically) (Dellinger and others, 2015, Frings and others, 2016).

Recently, Baronas and others (2018) presented a conceptually similar mass-balance model based on river solute Ge/Si ratios, δ^{30}Si, and germanium isotope ratios (δ^{74}Ge). Applied to a range of global rivers, including several of the world's largest catchments, their model predicts e_{sec}^{Si} spans from 0.19 to 0.79 (mean = 0.54), e_{org}^{Si} from 0.12 to 0.54 (mean = 0.32), and w^{Si} from 0.03 to 0.40 (mean = 0.14). Thus, at the global scale considered by Baronas and others (2018) only about 14 % of Si solubilized from parent rock appears in stream water as solutes, with the rest split roughly 60/40 between secondary clays and biogenic material. These results are remarkably similar to our independent Ge/Si-δ^{30}Si based mass-balance (table 4; fig. 6) despite different underlying assumptions and approaches. Specifically, Baronas and others (2018) use river chemistry and dissolved Ge δ^{74}Ge as additional constraints, and additionally solve for the isotope fractionations associated with clay formation and biological uptake (and thus δ^{30}Si and δ^{74}Ge of these phases). In contrast, we directly measure their composition and include these values as constraints in the mass-balance. It is noteworthy that this conclusion was largely corroborated in an intensely weathered, andesitic setting in lowland Costa Rica where measured clay and biomass compositions could further constrain the model (Baronas and others, 2020).

It is instructive to consider the nature of the fractionated solid. In our conceptualisation, it can be either secondary clays or plant material. Note that we use the term clay to include oxides and other phases formed as a result of silicate weathering reactions. Based on the median values of all successful Monte Carlo iterations, the export of secondary clays and the export of biogenic material are roughly equivalent: e_{sec}^{Si} is

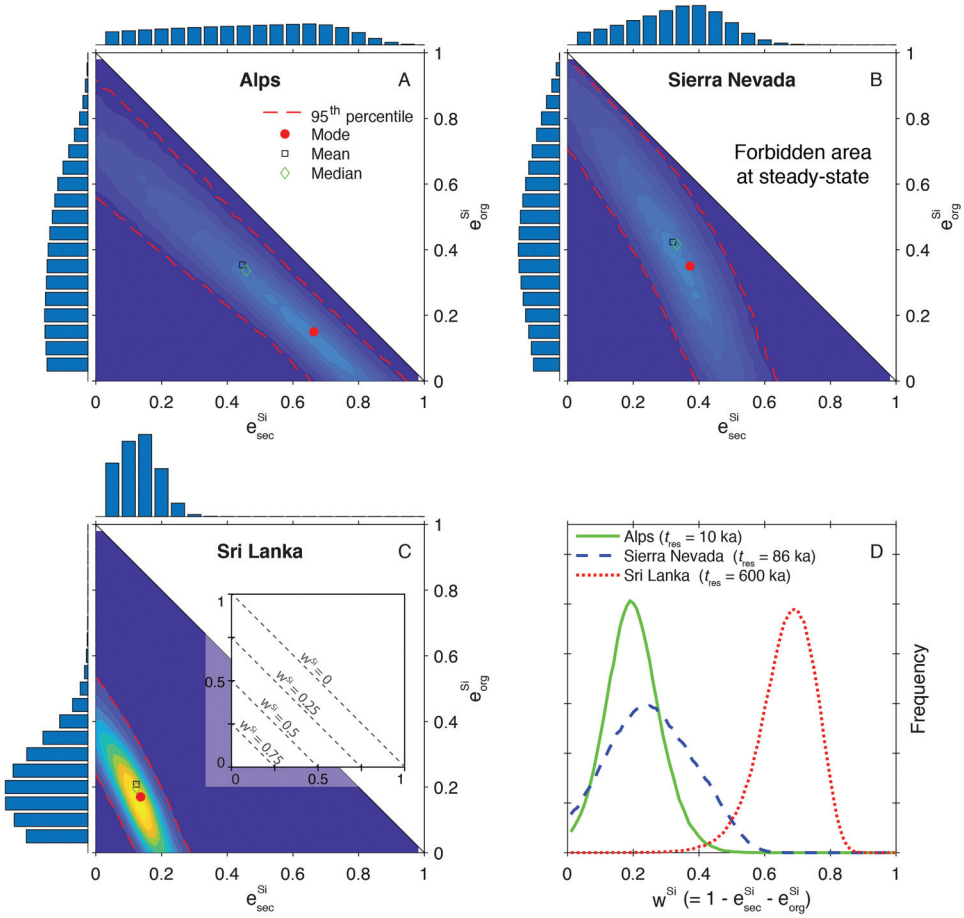

Figure 6. Density plots of solutions to mass-balance equations to estimate the mechanism of Si export (relative to Si solubilisation) in secondary solids (e^{Si}_{sec}), plant-derived solids (e^{Si}_{org}) and dissolved Si (w^{Si}) from the three sites (eq 15 – eq 17). Dashed red lines indicate the boundaries within which 95 % of all solutions fall, and red circles indicate median solutions. The color scale indicates the density of solutions to 10^6 randomly drawn input Ge/Si ratios and δ^{30}Si values, drawn from normal distributions defined by sample means and standard deviations (table 3, with the exception of Sierra Nevada waters where we prescribe a uniform distribution between 0 and 0.1). See also table 4 for results. Inset panel shows contours of w^{Si} (constant $e^{Si}_{sec} + e^{Si}_{org}$). The results show a) a decrease in w^{Si} with decreasing regolith residence time, that is, relatively greater fractionated solid export at short residence times, and b) an increase in the relative importance of biogenic Si export at high erosion rates.

ca. 1.4x higher than e^{Si}_{org} in the Alps, but 0.8x and 0.6x smaller in Sierra Nevada and Sri Lanka, respectively. The calculated export of biogenic material is surprisingly large, corresponding to median values of 35 ± 22 %, 43 ± 23 % and 21 ± 12 % of total solubilized Si in the Alps, Sierra Nevada and Sri Lanka, respectively. Based on these median values (fig. 6; table 4), Si exported in biogenic material is 171 %, 166 % and 29 % of dissolved Si export (that is, w^{Si}) in the Alps, Sierra Nevada and Sri Lanka. However, as figure 6A–C shows, essentially any combination of e^{Si}_{sec} and e^{Si}_{org} is plausible at the three sites: the 95th percentile contour intersects both axes at all three sites. This implies that the partitioning of Si export between clay minerals and biogenic material is poorly constrained. Nevertheless, we suggest these estimates of e^{Si}_{org} are

TABLE 4

The fate of solubilized Si at the three erodosequnce sites, derived by solving coupled Ge/Si-δ^{30}Si mass balance equations (Eqn. 15–Eqn. 17).

	Dimensionless quantities						t km^{-2} yr^{-1}		
	e_{sec}	e_{org}	w	$e_{org}/(e_{sec}+e_{org})$	e_{org}/w	DEE_{Na}^{Si}	W^{Si}	U^{Si}	E_{org}
Alps	0.46±0.23	0.34±0.22	0.20±0.08	0.42	1.71	0.49±0.50	2.06±1.36	2.34	3.51±3.62
Sierra Nevada	0.33±0.14	0.42±0.23	0.25±0.08	0.56	1.66	0.53±0.23	4.86±1.48	4.04	8.05±5.66
Sri Lanka	0.12±0.06	0.20±0.12	0.68±0.08	0.61	0.29	0.63±0.58	0.85±0.28	8.87	0.25±0.18
Baronas and others (2018), global rivers	0.54±0.17	0.32±0.12	0.14±0.11	0.63	2.29	--	--	--	--

Uncertainty estimates are given as median $\pm 1\sigma$ and result from a Monte-Carlo approach, solving the mass-balance 10^6 times using uncertainties as given in Table 3 (for Ge/Si) and Frings and others (2021a) (for δ^{30}Si). An independent, but conceptually similar, model for global rivers based on paired δ^{74}Ge-δ^{30}Si data is shown for comparison (Baronas and others, 2018). For comparative purposes, we show values for various Critical Zone metrics relating to Si fluxes: The Dissolved Export Efficiency (DEE), the river dissolved Si flux (W^{Si}), and the ecosystem Si fixation flux (U^{Si}) from von Blanckenburg and others (2021). See main text for details.

accurate, for two main reasons. First, our values agree with those of Baronas and others (2018), who present an independent δ^{74}Ge-δ^{30}Si mass balance for global rivers spanning a range of sizes, lithologies and climates. They derive e^{Si}_{org} estimates of 0.12 to 0.54, neatly bracketing our values. Second, when we rerun our analyses but make the assumption that only phytolith material is likely to erode (because they are more likely to survive redissolution), the results are largely unchanged. In this case, we prescribe a literature value of 0.5±0.1 μmol mol^{-1} for the biogenic material (based on data compiled in table A1). This produces estimates of e^{Si}_{org} of 34 %, 35 %, and 15 % of total solubilized Si in the Alps, Sierra Nevada and Sri Lanka, respectively. Further details are given in Appendix B, which details a sensitivity analysis. Overall, the conclusion that biomass Si erosion is roughly equal to, or greater than, dissolved Si export appears to be a robust prediction of coupled Ge and Si mass balance models.

A" missing" Si flux is found in plant material?.—Having quantified the partitioning of solubilized Si between biomass-erosion (e^{Si}_{org}), clay-erosion (e^{Si}_{sec}), and export of dissolved Si (w^{Si}), we can compare this result to estimates of weathering intensity $(W/D)^{Si}$. Note that unlike the term we introduce above (that is, $w = 1 - \left(E^{Si}_{org} + E^{Si}_{sec}\right)/S^{Si}_{prim}$) which considers the partitioning of Si after it is solubilized, $(W/D)^{Si}$ quantifies the net fraction of total denudation achieved chemically, that is, including erosion of primary minerals (eq 11). Here, we calculate weathering intensity $(W/D)^{Si}$ in three different ways. First, using the data of Frings and others (2021a), a silicon-specific weathering intensity can be quantified from isotope partitioning (Bouchez and others, 2013):

$$(W/D)^{\mathrm{Si}}_{\mathrm{isotope}} = \frac{\delta^{30}\mathrm{Si}_{\mathrm{sed}} - \delta^{30}\mathrm{Si}_{\mathrm{rock}}}{\delta^{30}\mathrm{Si}_{\mathrm{sed}} - \delta^{30}\mathrm{Si}_{\mathrm{diss}}} \tag{18}$$

where $\delta^{30}\mathrm{Si}_{\mathrm{sed}}$, $\delta^{30}\mathrm{Si}_{\mathrm{diss}}$ and $\delta^{30}\mathrm{Si}_{\mathrm{rock}}$ are the mean Si isotope ratios of all solid material leaving the catchment, of river solutes, and of bedrock, respectively. As done elsewhere, we assume that bulk topsoils are representative of river sediment (Bouchez and others, 2013). This expression is derived from the mass-balance in equation (4) and equation (5): at low weathering intensities, the isotope composition of the sediment approaches that of the rock, so the numerator tends towards zero. The term $(W/D)^{Si}_{isotope}$ takes values of 0.05, 0.10 and 0.39, in the Alps, Sierra Nevada, and Sri Lanka, respectively. Second, von Blanckenburg and others (2021) use an approach based on the ratio of measured river loads to total Si-specific denudation:

$$(W/D)^{Si}_{river} = \frac{Q[Si]_{diss}}{[Si]_{rock}D} \tag{19}$$

where Q is river runoff (m yr^{-1}), $[Si]_{diss}$ is Si concentration (mol m^{-3}) in river water, $[\mathrm{Si}]_{\mathrm{rock}}$ is the concentration of Si in bedrock (mol kg^{-1}), and D is denudation rate (kg m^{-2} yr^{-1}) from cosmogenic *in situ* ^{10}Be (von Blanckenburg and others, 2021). $(W/D)^{Si}_{river}$ is similar to $(W/D)^{\mathrm{Si}}_{\mathrm{isotope}}$, equating to 0.06, 0.08 and 0.18 in the Alps, Sierra Nevada, and Sri Lanka, respectively. Both these estimates are substantially lower than a third metric of weathering intensity, $(W/D)^{Si}_{regolith}$, that provides an estimate of net Si lost from regolith by using representative $-\tau_{Si}$ values (eq 3) and results in 0.34, 0.35, and 0.52 for the Alps, Sierra Nevada, and Sri Lanka, respectively (von Blanckenburg and others, 2021). In other words, there is a discrepancy between metrics of weathering intensity that rely on measurement of Si dissolved flux exported in a river (Si flux

and/or δ^{30}Si; that is, $(W/D)^{Si}_{isotope}$ and $(W/D)^{Si}_{river}$) and those that reflect the net loss of Si from the regolith (that is, $(W/D)^{Si}_{regolith}$).

Conceptually, this discrepancy is related to the observation that 'Dissolved Export Efficiency' (DEE) is often less than unity for many elements. The DEE is a metric introduced by Uhlig and others (2017) and expanded on by von Blanckenburg and others (2021) and Bouchez and von Blanckenburg (2021). The DEE metric quantifies the observed riverine export of a solute from a catchment relative to its release by weathering from regolith. In its simplest form, a silicon specific DEE can be expressed as (Uhlig and others, 2017):

$$\mathrm{DEE}^{Si} = \frac{(W/D)^{Si}_{river}}{(W/D)^{Si}_{regolith}} \tag{20}$$

Because $(W/D)^{Si}_{river}$ integrates over the period of river load monitoring, maximally a few decades, whereas $(W/D)^{Si}_{regolith}$ integrates over regolith residence time – typically $>10^3$ yrs (table 1), timescale differences may arise. To eliminate these, both fluxes are normalised to a conservative element like Na:

$$\mathrm{DEE}^{Si}_{Na} = \frac{(W/D)^{Si}_{river} \Big/ (W/D)^{Si}_{river}}{(W/D)^{Si}_{regolith} \Big/ (W/D)^{Si}_{regolith}} = \frac{\left(\frac{[Si]}{[Na]}\right)_{river} \Big/ \left(\frac{[Si]}{[Na]}\right)_{rock}}{\tau^{Si}_{Zr} \Big/ \tau^{Na}_{Zr}} \tag{21}$$

Na is selected since it is neither incorporated into secondary minerals, nor taken up by plants to an appreciable degree. The rationale is that any deviation in DEE^{Na} reflects the difference in timescales the two estimates of W/D integrate over. A DEE^{Si}_{Na} index below one implies that there is a 'missing' flux of the element: less is being exported as solute than expected based on soil or regolith chemistry. For Si, the best estimate of DEE (that is, from eq 21) is 0.49, 0.53 and 0.63 in the Alps, Sierra Nevada and Sri Lanka, respectively (von Blanckenburg and others, 2021). This means the dissolved Si flux is about half of that expected based on regolith geochemistry. This deficit implies that dissolved Si is removed from regolith (as required by the τ_{Si} values) but does not reappear in the river. Expressed alternatively, the Si/Na ratio of mass removed from the regolith is higher than that observed in stream water. Discounting a timescale mismatch, which the Na normalisation (eq 21) aims to account for, one possible explanation (see von Blanckenburg and others (2021) for details, and other potential explanations) is that the Si is utilised by plants, and that erosion of biogenic material is responsible for its loss. In support of this hypothesis, note that the existence of $\mathrm{DEE}^{Si} \approx 0.5$, and the prediction made here that $e^{Si}_{org} \approx w^{Si}$ (see table 4), are internally consistent.

Magnitude and mechanisms of biomass erosion.—The estimates of e^{Si}_{org} introduced above and in table 4 are non-dimensional but can be scaled by the dissolved Si export fluxes presented in von Blanckenburg and others (2021). For the Alps, Sierra Nevada, and Sri Lanka, these are 2.06 ± 1.36, 4.86 ± 1.48, and 0.85 ± 0.28 t km^{-2} yr^{-1}, respectively. They are calculated as the product of monitored river discharge and dissolved Si concentration. This yields E^{Si}_{org} estimates of about 3.51 ± 3.62 t km^{-2} yr^{-1} in the Alps, 8.05 ± 5.66 t km^{-2} yr^{-1} in Sierra Nevada, and 0.25±0.18 t km^{-2} yr^{-1} in Sri Lanka, with all uncertainties propagated in quadrature (table 4). Both the estimates

of river dissolved Si flux, and the results of our geochemical inversion (section 'Quantifying Si export by river solutes and in eroded clays and biomass') have large relative uncertainties (expressed as 1σ), though we have no reason to suspect they are biased. We consider these propagated uncertainties on the magnitude of the biomass erosion flux of Si to be conservatively large. The uncertainties notwithstanding, are these numbers feasible? As a first-order sanity check, we can compare them to the mass of biogenic silica available to be eroded. Total biomass production at these sites, as approximated by gross primary productivity (GPP) estimates, is 779 ± 9, 1350 ± 30 and 2560 ± 50 t km^{-2} yr^{-1} (Jung and others, 2019, von Blanckenburg and others, 2021). Si concentrations are heterogeneous in plant biomass, and root pools are notoriously hard to access for measurement. Our sampling therefore does not allow a weighted average to be made, so we take a representative value of 0.3 wt% from Carey and Fulweiler (2012) for illustrative purposes. This yields ecosystem Si fixation rates (U^{Si}) of about 2.3, 4.0 and 8.9 t km^{-2} yr^{-1} in the Alps, Sierra Nevada, and Sri Lanka, respectively. Note that an estimated concentration of 0.3 % for the grass taxa of the Alps may be an underestimate since grasses typically actively accumulate Si. The predicted E^{Si}_{org} fluxes are larger than U^{Si} in the Alps and Sierra Nevada sites (by about a factor of 1.6 and 2.0), but we consider that, given the uncertainties associated with for example, plant Si concentration, GPP, and the results of our mass-balance model (fig. 6; table 4) that predicted E^{Si}_{org} and calculated U^{Si} are equivalent. A precise quantification awaits more detailed mass-balance work, but the implication is clear: the majority of Si fixed by plants in the Alps and Sierra Nevada ecosystems is eroded rather recycled. This differs from previous work (for example, Derry and others, 2005) that argues that a large fraction of stream dissolved Si has passed through a biogenic pool but was ultimately re-dissolved before export. For the Sri Lanka site, only about 3% of annual plant Si fixation is predicted to be eroded, which is in line with the general 'recycling' character of this ecosystem (von Blanckenburg and others, 2021). While the ecosystem Si fixation rates are 'back-of-the-envelope' calculations, they corroborate the feasibility of the calculated E^{Si}_{org} fluxes.

The inference that E^{Si}_{org} is of a similar magnitude as U^{Si} in two of three sites is surprising. Previous work has emphasised the recycling of plant biogenic silica as a nutrient retention strategy (for example, de Tombeur and others, 2020). Further support for substantial E^{Si}_{org} comes from a) the observation of a DEE < 1 (von Blanckenburg and others, 2021; see above), b) independent mass-balance calculations in other catchments that also predict a substantial erosional flux of biogenic Si (Baronas and others, 2018, Baronas and others, 2020), and c) the observation (Frings and others, 2015, 2016) that Si/Na in river waters is often much lower than that expected based on source rock Si/Na and typical net weathering reaction stochiometries. Using erodosequence examples from Frings and others (2021a; their table 5), between 35 and 80 % of Si solubilized should be retained in secondary clays, depending on the reaction. For a typical granite Si/Na molar ratio of *ca.* 3 to 4 (ignoring an inert quartz component) river water should thus generally be > 1 mol/mol Si/Na. This is often not the case (Frings and others, 2016, their fig. 8), even after accounting for Na from rainwater and evaporites, which implies Si removal from solution into solid, but non-clay phases.

The question then arises: what is the mechanism of such substantial erosion of biogenic silica? We identify at least five non-exclusive pathways: (i) the erosion of fine-grained biomass debris, (ii) the erosion of coarser biomass, (iii) anthropogenic 'erosion', via logging, (iv) the appearance of biomass erosion, via non-steady-state biomass aggradation, and (v) in-stream production of biogenic silica (bSi) by diatoms or other primary producers.

The first potential export mechanism is the erosion of fine-grained biogenic silica phases, including Si in phytoliths or otherwise associated with particulate organic matter originally contained in the foliage of plants. This fulfils the constraint that Si is removed from regolith (as required by the τ_{Si} values) without allowing it to reappear in the dissolved form in the river. Because calculated $e_{org}^{Si} \approx w^{Si}$, then the ratio of biogenic silica in river sediment to dissolved Si should be around one. This is larger than typically seen in selective leaches of river suspended sediment (Conley, 1997; Carbonnel and others, 2009; Smis and others, 2011; Clymans and others, 2013; Frings and others, 2014). These analyses target amorphous Si phases (assuming this is dominantly biogenic silica) with basic leaching solutions and typically yield Si concentrations equivalent to around 10 to 20% of river dissolved Si. In the Ganges and its tributaries, Frings and others (2014) show that extrapolation based on concentrations in surface-water suspended sediment may underestimate total fluxes, and thus depth-integrated water-column sediment fluxes are needed (compare with Bouchez and others, 2011). Estimates of suspended load flux may underestimate true solid transport because of the stochastic nature of sediment transport, particularly in mountainous headwater catchments. Scaling biogenic silica export by independent estimates of river sediment flux (for example, from *in situ* ^{10}Be) may yield more reliable values but requires knowing the fraction of river sediment that is biogenic silica. The available data from large rivers (including the Ganges, Amazon, Huang He and Changjiang) suggest a value of around 1 to 2 % of river sediment may be reasonable (Conley, 1997, Frings and others, 2014, Liu and others, 2016). Taking a global sediment flux of 15.2 ± 2.8 Gt yr^{-1} (Wittmann and others, 2020), then $2.5 – 5.0 \times 10^{12}$ mol bSi) is estimated to be delivered to the global ocean. This is equivalent to about 40 to 80 % of river dSi flux (Beusen and others, 2009). Making the assumption that the river bSi flux is relatively larger in headwater catchments (that is, before phytoliths have time to dissolve), then we suggest this exercise corroborates the feasibility of $E_{org}^{Si} \geq WSi$.

A second (and related) biomass-export mechanism is the export of coarse organic particulates, not typically included in river sediment fluxes. Recent evidence suggests it is an important mass flux term, especially in small mountain headwater streams akin to those investigated here (Wohl and others, 2012; Turowski and others, 2016; Kramer and others, 2017). Its importance in carbon export and burial is receiving attention (West and others, 2011; Lee and others, 2019), but other elements contained in the coarse particulates have been neglected. Turowski and others (2016) estimated coarse biomass fluxes at Erlenbach, a Swiss Prealps site, comparable in climate, elevation, and vegetation to our Alps site, with three different methods. They derive an annual flux of 87.7 ± 51.9 t C km^{-2} yr^{-1} and note that rare flood events dominate this term. Assuming that carbon is approximately 50 % of the total mass, and silicon about 0.3 % (see above), this yields an estimate of E_{org}^{Si} (in coarse biomass only) of *ca.* 0.5 t Si km^{-2} yr^{-1} for a small, mountainous catchment. Subsequent work suggests the Ehlenbach coarse biomass fluxes are towards the high end of the spectrum of plausible values (Bunte and others, 2016), so the estimate of coarse E_{org}^{Si} is likely also an upper limit. We tentatively conclude that erosion of coarse biomass debris is a small but non-negligible vector of Si export from catchments. Additionally, the Alps site is located on grasslands that are grazed by goats in the summer. Recent work has shown how animals can be unexpectedly large vectors of Si and other nutrient fluxes (Schoelynck and others, 2019), so their repackaging of grass biomass into faecal pellets may increase the erosional efficiency.

A third biomass-export mechanism is the logging or harvesting of catchment biomass, which would have the same impact: mass would be being removed from the catchment without appearing in river sediment. This is what de Oliveira Garcia and

others (2018) term a 'negative nutrient budget.' It is well established for silicon cycling that in agricultural systems crop harvesting is a substantial term, which can be greater than, for example, input from weathering (Sferratore and others, 2005; Vandevenne and others, 2012; Klotzbücher and others, 2018), so even relatively small harvests could impact Si export if maintained over sufficiently long timescales. To our knowledge, there is no large-scale modern-day logging or any form of harvesting that removes biomass from the catchment at our sites, though there has been in the past (see below). We discount this as a mechanism of E_{org}^{Si} in the three erodosequence sites.

The fourth mechanism we consider is the growth of a Si pool within the catchment, rather than export of that pool *per se*. If the ecosystem is growing and living (or dead) biomass is accumulating (Struyf and others, 2010; Wohl and others, 2012; Clymans and others, 2016), this would be equivalent to an export flux with biogenic composition from the soil/regolith. For the three sites investigated here, vegetation the Alps is mostly grasses, so there is not much scope for transient ecosystem Si accumulation. At the Sierra Nevada site the *Pinus ponderosa* forests were nearly entirely clear-cut in the late 19th century and have experienced logging of some form until the 1960s (Uhlig and others, 2017). Although a stable vegetation density is likely now attained, there may still be a slight net-aggradation of above- and below-ground (woody) biomass. As a rainforest reserve, the Sri Lanka site has not been affected by agricultural or forestry uses (Hewawasam and others, 2013) and we assume the ecosystem is at steady-state. Some minor net biomass-Si aggradation might be occurring in Sierra Nevada, but is unlikely elsewhere.

Finally, in-stream production of diatoms is a potential explanation for a regolith removal flux that does not appear in stream waters. However, point-counting of river biogenic Si particles tends to suggest the dominance of phytolith over diatoms in contributions to total river biogenic silica, in particular in small rivers (Cary and others, 2005; Zang and others, 2016; Schoelynck and others, 2019). The only systems where diatoms are the most abundant biogenic silica particles are dams that provide the low-turbidity environments needed for diatoms to thrive (Meunier and others, 2015; Ran and others, 2016; Baronas and others, 2018). Coupled with the short stream lengths, turbid flow, and low P concentrations (von Blanckenburg and others, 2021), we discount the possibility of in-stream biogenic silica production by diatoms or other silicifying organisms.

Overall, the most the most likely dominant mechanism of erosion of biomass seems to be the removal of Si in phytoliths or fine-grained particulate organic carbon phases produced by degrading plant biomass. We note that previous work has highlighted how this fine fraction can be preferentially mobilised during overland flow, especially at low magnitude erosive events, due to its size and density (Clymans and others, 2015). This seems to operate particularly efficiently (that is, most biogenic Si in litterfall is eroded) in the steep Alps and Sierra Nevada sites, and less efficiently (only a small fraction of litterfall Si is eroded) at the Sri Lanka site. This is consistent with stand-level investigations of Si recycling efficiency in temperate ecosystems vs. tropical ecosystems (Lucas, 2001). Repackaging of biogenic silica into faecal pellets in the Alps, and aggradation of biomass at the Sierra Nevada sites, may also contribute to the interpretation that a substantial fraction of biologically fixed Si is lost via erosion. Logging and in-stream diatom growth are unlikely to be a mechanism of Si export from the studied catchments, though may be important elsewhere. Others have demonstrated the importance of biological activity to Si cycling at the soil-profile scale (for example, Li and others, 2020); we suggest here this importance extends to the export of Si at the catchment scale.

CONCLUSIONS

We have quantified Ge/Si ratios in multiple ecosystem pools (bedrock, bulk soil and saprolite, the clay size fraction, plant biomass and stream water solutes) at three sites spanning a gradient of erosion rates and thus weathering intensities. This data, in combination with silicon isotope data on the same samples presented in a companion paper, permits insight into the relative partitioning of Ge and Si at the Earth's surface. Specifically, we demonstrate that:

- A compilation of literature data shows that primary mineral specific Ge/Si ratios can vary between < 0.5 to > 6 μmol mol^{-1}. This underscores the need to consider individual mineral weathering rates, particularly in kinetically limited settings.
- Ge discrimination relative to Si during biological uptake is not a widespread plant strategy. Instead, some plants appear to preferentially take up Ge, some with no discrimination, and some discriminate against Ge. The common observation of low Ge/Si phytoliths must therefore be explained by processes that occur internal to the plant.
- Ge is preferentially incorporated into secondary clays relative to Si, with exchange coefficients at the catchment scale between 5.4 to 65, extending the range of values derived from other settings.
- Because these exchange coefficients are consistently greater than unity, Ge/Si ratios in secondary clays are more sensitive tracers of weathering regime than Ge/Si ratios in stream solutes, the more conventional proxy. This conclusion is arrived at both empirically (fig. 2 and fig. 3) and via a mass-balance framework (section 'Application of Coupled Ge/Si-δ^{30}Si Mass Balance Models' and eq 9 and eq 10).

Beyond this, we show how a series of coupled Ge/Si and silicon isotope mass balance equations can be solved to quantify in which form Si is exported from a catchment. The results define a decrease in weathering congruency with decreasing regolith residence time. They also require that between 18 % to 39 % of Si that is solubilized from primary minerals is exported from the catchment in a biogenic form. This is a surprisingly large fraction, but is consistent with independent lines of evidence, and is feasible given the currently available constraints.

ACKNOWLEDGEMENTS

We thank Julien Bouchez for discussion and a constructive review of an earlier version of the manuscript, Kevin Norton for the introduction to on the Swiss Alps field site, Jeannie Dixon for the introduction to the Sierra Nevada field site, and Tilak Hewawasam for the introduction to the Sri Lanka field site. Jan Schüssler, Jeannie Dixon, Julien Bouchez and Tilak Hewawasam helped with sampling. We thank David Uhlig for discussions and contributing background data for the Sierra Nevada site. Jutta Schlegel, Josifine Holtz and Daniel Frick are thanked for assistance with analyses at the HELGES laboratory. We are indebted to Alida Perez-Fodich and J. Jotautas Baronas for their thorough, constructive, and useful reviews that helped us improve our manuscript.

APPENDICES

Appendix A: Previous Determinations of K_D^{veg} for the Ge/Si System

TABLE A1

Summary of previous work investigating Ge discrimination relative to Si during plant uptake

	Reference	Setting	Common name	Scientific name	Solution Ge/Si (μmol mol^{-1})	Plant or Phytolith Ge/Si (μmol mol^{-1})	$(Ge/Si)_{plant}$ / $(Ge/Si)_{solution}$	Preparation notes
Laboratory	D09	Hydroponic solutions	Banana	*Musa acuminata*	--	--	ca. 1	K_D tracked by trends in growth solution Ge and Si concentrations through time. Ge present in high concentrations (starting concentration: 0.32 mg l^{-1}).
	R06	Hydroponic solutions	Wheat	*Triticum aestivum*	--	--	ca. 1	K_D tracked by trends in growth solution Ge and Si concentrations through time; Ge concentrations 10^6 higher than natural.
	B07	Hydroponic solutions	Western wheatgrass, roots	*Agropyron smithii*	0.50	0.12	0.24	Plant washed, ashed,washed in warm, 1M hydrochloric acid and hot 30 % hydrogen peroxide.
			Western wheatgrass, above ground	*Agropyron smithii*	0.50	0.09	0.18	
			Little bluestem, above ground	*Schizachyrium scoparium*	0.50	0.09	0.17	
			Big bluestem, above ground	*Andropogon gerardii*	0.50	0.07	0.14	
		Greenhouse pots	Western wheatgrass, above ground	*Agropyron smithii*	0.25	0.11	0.43	Plant washed, ashed, washed in warm 1M hydrochloric acid and hot 30 % hydrogen peroxide. Plants average of two experimental soils ('potting' and 'field' soil). Soil water from 'saturated paste equilibriation'
			Little bluestem, above ground	*Schizachyrium scoparium*	0.25	0.12	0.47	
			Big bluestem, above ground	*Andropogon gerardii*	0.25	0.11	0.43	
			Blue grama, above ground	*Bouteloua gracilis*	0.25	0.10	0.41	
			Buffalo grass, above ground	*Buchloe dactyloides*	0.25	0.13	0.51	
			Indian ricegrass, above ground	*Oryzopsis hymenoides*	0.25	0.09	0.37	
Field	D09	Sandy clay soils; botantical garden	Horsetail roots	*Equisetum kamchaticum*	1.92	16.40	8.54	Ashing followed by $LiBO_2$ fusion with no intermediate acid leaching step. Clay correction applied to root samples, assuming no Al in roots. Ge/Si taken as unweighted mean of all samples, separated into roots and all other plant parts. Solution Ge/Si value taken as Ge/Si of bulk soil.
			Horsetail, above ground	*Equisetum kamchaticum*	1.92	0.11	0.06	
			Horsetail, roots	*Equisetum telmateia*	1.73	8.44	4.88	
			Horsetail, above ground	*Equisetum telmateia*	1.73	1.06	0.61	
	D05	Basalt, Hawaii	Hawaiian tree fern	*Cibotium chamissoi*	3.39	0.12	0.04	Phytoliths extracted chemically from plant material by microwave digestion in HNO_3 and H_2O_2 at 180 °C for 10 minutes, before digestion in 2M NaOH. Data taken as unweighted mean of all samples; solution mean of all samples (stream waters much lower)
			Hawaiian tree fern	*Cibotium glaucum*	3.39	0.07	0.02	
			Old World forked fern	*Dicrauopteris linearis*	3.39	0.05	0.01	
			Hawaiian fern	*Diplazium* spp.	3.39	0.09	0.03	
	D09	Basalt, Cameroon	Banana, roots	*Musa acuminata*	--	2.30	--	Ashing followed by $LiBO_2$ fusion with no intermediate acid leaching step. Clay correction applied to root samples, assuming no Al in roots. Plant Ge/Si taken as unweighted mean of all samples.
			Banana, above ground	*Musa acuminata*	--	0.18	--	

TABLE A1
Continued

Reference	Setting	Common name	Scientific name	Solution Ge/Si (µmol mol^{-1})	Plant or Phytolith Ge/Si (µmol mol^{-1})	$(Ge/Si)_{plant}$ / $(Ge/Si)_{solution}$	Preparation notes
M16	Shale, SSHCZO	Sugar Maple, above ground	*Acer saacharum*	1.58	0.03	0.02	Microwave digestion with HNO_3 and H_2O_2 at 180 °C for 10 minutes, following protocol from Parr and others (2001). Presumably followed by NaOH dissolution (though not stated). Data taken as unweighted mean of all samples.
		Chestnut Oak, above ground	*Quercus prinus*	1.58	0.03	0.02	
		Red Oak, above ground	*Quercus rubra*	1.58	0.58	0.36	
W12	Santa Cruz Chronosequence	Grass species; above ground	--	0.55	0.08	0.15	No detailed description given, but samples were ashed then digested in acid in an autoclave. Solution Ge/Si from unweighted mean of all reported porewater samples.
C10	Granite, France	Douglas Fir,above ground	*Pseudotsuga menziesii*	1.30	0.20	0.15	Phytoliths extracted with a mixture of HNO_3 and H_2O_2, followed by $LiBO_2$ fusion. Soil solutions from ceramic lysimeters at 60 cm at -400 hPa.
		Norway spruce, above ground	*Picea abies*	1.00	0.10	0.10	
		Black Pine, above ground	*Pinus nigra*	1.20	1.50	1.25	
		European Beech,above ground	*Fagus sylvatica*	1.40	0.20	0.14	
		Oak, above ground	*Quercus sessiliflora*	1.10	0.30	0.27	
L10	Granite, Puerto Rico	Sawgrass	*Cladium jamaicense*	2.60	0.53	0.20	Microwave digestion with HNO_3 and H_2O_2 at 180 °C for 10 minutes. Washed five times in H_2O, phytoliths dissolved in NaOH. Plant data as given; solution data from mean of soil-water data from lysimeters installed at three profiles.
		Sierra palm	*Prestoea montana*	2.60	0.12	0.05	
		Pumpwood	*Cecropia schreberiana*	2.60	0.03	0.01	
		Grass	--	2.60	0.21	0.08	
		Common fern	--	2.60	0.20	0.08	
		Fire fern	Gleicheniaceae	2.60	0.11	0.04	
		Tree fern	*Cyathea arborea*	2.60	0.17	0.07	
B05				0.69	0.31	0.45	North American grass species, phytolith extracts. Data cited in Blecker and others (2007) without analytical details.
B20	Andesite, Costa Rica	Tropical rainforest	--			0.62±0.28	Geochemical inversion of soil water, soil, and plant elemental and isotopic composition.
This study	Alps			0.51	3.1	6.08	
	Sierra Nevada			< 0.1	2	> 20	
	Sri Lanka			0.46	2.42	5.26	

References: D09: Delvigne and others (2009) R06: Rains and others (2006) B07:Blecker and others (2007) D05: Derry and others (2005) M16: Meek and others (2016) W12: White and others (2012) C10: Cornelis and others (2010) L10: Lugolobi, Kurtz, and Derry (2010) B05: Blecker (2005), cited in Blecker and others (2007); B20: Baronas and others (2020).

Appendix B: Sensitivity Analysis of Coupled Ge/Si-δ^{30}Si Mass Balance Model

The Ge/Si-δ^{30}Si mass-balance presented in the main text predicts 80 %, 75 % and 32 % of Si solubilized from parent rock is exported as fractionated solids that form in the weathering zone in the Alps, Sierra Nevada, and Sri Lanka, respectively. Of these fractionated solids, 58 %, 44 %, and 39 % are exported as biomass (table 4). The feasibility and implications are discussed in the main text; here we present a simple sensitivity analysis to assess (i) the robustness of the conclusions, and (ii) identify which parameters need to be most tightly constrained in future field-campaigns.

As we highlight in the main text, the modelled ratio e^{Si}_{org}/w^{Si} is larger than the available river amorphous-silica concentrations would suggest. Might this prediction simply be an artefact of the model? We explore this further by prescribing e^{Si}_{org} in equations (15)–(17) in the main text to be a constant fraction of w^{Si} (taking 0.16 after Conley (1997)) and solving instead for one of the eight ratios used as input for the mass-balance ($\delta^{30}Si_{rock}$, $\delta^{30}Si_{sec}$, $\delta^{30}Si_{org}$, $\delta^{30}Si_{diss}$, $\left(\frac{Ge}{Si}\right)_{rock}$, $\left(\frac{Ge}{Si}\right)_{sec}$, $\left(\frac{Ge}{Si}\right)_{org}$, or $\left(\frac{Ge}{Si}\right)_{diss}$), holding the rest constant. Although this exercise does not allow for co-variation in these terms, it allows the robustness of the conclusion that e^{Si}_{org} is large to be assessed.

Solving for δ^{30}Si values in clays, plant material, or in river water when $e_{org} = 0.16 \cdot w$ requires that the measured values would have to be incorrect by ≥ 1 ‰ to close the mass-balance. We thus rule out bias in these values. Parent material δ^{30}Si would have to be positive to produce a closed mass-balance, yet essentially all measurements to date of granitoid rocks cluster consistently around -0.2 to -0.3 ‰ (Savage and others, 2012, 2013b, 2014), so we also rule this out. Note that any apparent or real fractionation during dissolution would operate in the other direction, that is, to preferentially release the lighter Si isotopes (for example, Ziegler and others, 2005a; Frings and others, 2021a). Thus, the conclusion $e^{Si}_{org} \geq w^{Si}$ is insensitive to assumptions about δ^{30}Si of the various pools.

Solving the mass-balance equations for $\left(\frac{Ge}{Si}\right)_{sec}$ or $\left(\frac{Ge}{Si}\right)_{diss}$ when $e_{org} = 0.16 \cdot w$ produces negative Ge/Si ratios, so this is also not a plausible explanation. However, possible adjustments to the Ge/Si ratios of parent material or clay minerals would allow the mass-balance to be closed. The clay size fraction would be required to have a ratio *ca.* 1 μmol mol^{-1} lower, or the rocks *ca.* 0.5 μmol mol^{-1} higher, to produce a result that is consistent with the Conley (1997) estimate of amorphous Si concentrations in rivers. As detailed in our companion paper (Frings and others, 2021a), silicon isotope ratios can differ in rock-forming minerals by a substantial amount (0.4 to 0.8 ‰ at the erodosequence sites). If these differentially undergo weathering, then the isotope ratio of Si released to solution will not be equal to bulk rock. Although bulk rock Ge/Si is similar at the three sites (table 3), the same is true for Ge/Si ratios (see compilation in main text, section 'Ge and Si partitioning in the Critical Zone'). It is plausible that preferential weathering of biotite relative to less mafic minerals releases Si with a higher Ge/Si ratio than the bulk rock, closing the mass-balance with a biomass export flux in line with expectations. However, we tentatively discount this explanation, since (i) the high Ge/Si minerals tend to be a small fraction of total bedrock Si (Frings and others, 2021a), and (ii) primary mineral dissolution is relatively complete at the Sierra Nevada and Sri Lanka sites, meaning bulk-rock must be a good approximation of the Ge/Si ratio of solubilized Si. Preferential weathering of high Ge/Si mafic phases may be part of the explanation in the Alps site: future work could seek to constrain inter-mineral Ge/Si differences here. We also discount a bias on the Ge/Si ratio of the clay fraction, since we observe these ratios tend to increase towards the top of the regolith profiles. This means that if there is a bias on $\left(\frac{Ge}{Si}\right)_{sec}$, it is in the

TABLE A2

Results of sensitivity test to assess robustness of the coupled Ge/Si-δ^{30}Si mass balance model, when we assume the non-phytolith, high Ge/Si pool of Si in plants is much more readily remineralised and thus the exported material consists only of phytoliths.

	e_{sec}	e_{org}	w	$e_{org}/(e_{sec}+e_{org})$	e_{org}/w
Alps	0.47±0.15	0.34±0.15	0.18±0.07	0.42	1.84
Sierra Nevada	0.39±0.08	0.35±0.16	0.26±0.12	0.47	1.34
Sri Lanka	0.17±0.04	0.15±0.09	0.68±0.08	0.48	0.22

Here we assume the non-phytolith, high Ge/Si pool of Si in plants is much more readily remineralised and thus the exported material consists only of phytoliths. In this case, we prescribe $(Ge/Si)_{org} = 0.5$ based on typical phytolith values compiled in Table A1.

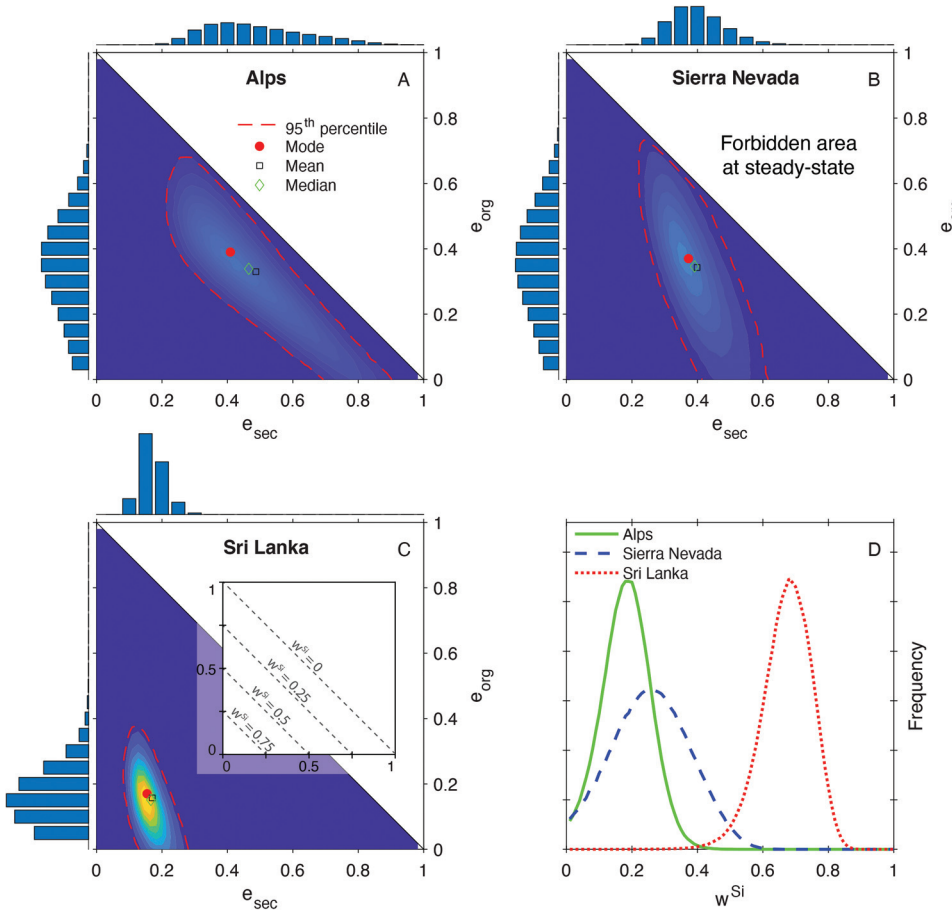

Figure A1. Results of Ge/Si-δ^{30}Si geochemical mass balance when prescribing $\left(\frac{Ge}{Si}\right)_{org} = 0.5\pm0.1$ (based on values compiled in Appendix table A1). Some of the higher e^{Si}_{org} scenarios in figure 6 are no longer possible, but the model prediction of median e^{Si}_{sec} and w^{Si} are largely similar (Appendix table A2). For further details, see figure 6.

wrong direction. Overall, it is difficult to close the mass-balance when imposing the constraint that $e_{org} = 0.16 \cdot w$.

Finally, we note that these conclusions are relatively insensitive to the Ge/Si ratio of organic material (fig. A1; table A2). Making the assumption that phytoliths are more refractory and thus more likely to be eroded than the putative Ge-rich organic complex (Kaiser and others, 2020), the values of the term $\left(\frac{Ge}{Si}\right)_{org}$ would instead be in the range of those in table A1 derived from phytolith extracts. Using an arbitrary but representative value of 0.5±0.1 μmol mol^{-1} yields $\left(E_{org}+E_{sec}\right)/S = 0.82$ in the Alps, 0.74 in Sierra Nevada, and 0.32 in Sri Lanka. Erosion of biogenic material is calculated to be remarkably similar to the values derived using measured bulk plant Ge/Si: e_{org} = 0.34, 0.35 and 0.15, along the Alps-Sierra Nevada-Sri Lanka transect. This crude sensitivity analysis suggests that the conclusion that biomass erosion is a substantial fraction of Si export from a catchment is robust, as independently validated elsewhere (Baronas and others, 2018, Baronas and others, 2020)

Appendix C: A Silicon Isotope Mass-Balance to Predict Plant Biomass Erosion

The mass-balance framework presented by Bouchez and others (2013) shows that:

$$\frac{\delta^{30}Si_{diss} - \delta^{30}Si_{rock}}{\overline{\Delta^{Si}}} = \frac{1 - CDF}{-\tau^{Si}_{prim}} \cdot \frac{[Si]_{sec}+[Si]_{org}}{[Si]_{rock}} \tag{S1}$$

where δ^{30}Si is the silicon isotope ratio of the dissolved phase and rock (subscripts 'diss' and 'rock'), $\overline{\Delta}^{Si}$ is the weighted average fractionation associated with all processes forming new Si-bearing solids, and CDF is a zirconium-based index of weathering intensity after Riebe, Kirchner, and Finkel (2003). The term τ^{Si}_{prim} is related to the term τ_{Si}, the silicon mass-transfer coefficient (Brimhall and Dietrich, 1987, von Blanckenburg and others, 2021) but indexes loss only from primary minerals, rather than the net effect of primary mineral dissolution and secondary mineral precipitation. See Bouchez and others (2013), their equation (16), for more detail. With the exception of τ^{Si}_{prim}, $\overline{\Delta}^{Si}$, and $[Si]_{org}$, all terms are empirically constrained at the Alps-Sierra Nevada-Sri Lanka erodosequence, with values from von Blanckenburg and others (2021) for CDF (0.31, 0.36, 0.50) and Frings and others (2021a) for δ^{30}Si values (-0.36 ±0.10, −1.33 ±0.50 and -2.03 ±0.31 ‰), and Si concentrations in clays (9210 ±6530, 22300 ±15100 and 26800 ±10700 μg g^{-1}). We take the plant and clay fractionations as derived in Frings and others (2021a) as upper- and lower- limits for the value of $\overline{\Delta^{Si}}$ (their tables 6 and 7, spanning a range from −3.36 ± 0.51 ‰ to −1.12 ± 0.20 ‰). Note that the $\overline{\Delta^{Si}}$ can also be derived from rock and river δ^{30}Si and Si/Na ratios to define f^{Si}_{solid} (for example, Hughes and others, 2013; Frings and others, 2015; Baronas and others, 2018), though this makes little difference to the results. Finally, τ^{Si}_{prim} is defined as:

$$\tau^{Si}_{prim} = \frac{[Si]_{prim}}{[Si]_{rock}} \times \frac{[Zr]_{rock}}{[Zr]_{soil}} - 1 \tag{S2}$$

where $[Si]_{prim}$ is the Si concentration of silicon remaining in rock that is hosted by primary minerals. By making the substitution that $[Si]_{prim} = [Si]_{bulk} - [Si]_{sec} - [Si]_{org}$, we can solve equation (S1) for $[Si]_{org}$, using a Monte-Carlo approach to propagate

TABLE A3

Results of a solely silicon-isotope based mass-balance to predict the relative partitioning of Si export between clays and biomass. Units are g Si per gram bulk soil

	$[Si]_{bulk}$	$[Si]_{prim}$	$[Si]_{sec}$	$[Si]_{org}$	$[Si]_{org}/[Si]_{sec}+[Si]_{org}$
Alps	0.319 ± 0.007	0.288 ± 0.019	0.010 ± 0.006	0.021 ± 0.016	0.674 ± 0.638
Sierra Nevada	0.282 ± 0.025	0.269 ± 0.034	0.024 ± 0.016	0.043 ± 0.026	0.646 ± 0.495
Sri Lanka	0.306 ± 0.010	0.215 ± 0.032	0.027 ± 0.011	0.010 ± 0.029	0.268 ± 0.817

uncertainties in parameter values. This approach yields estimates of Si concentrations bound to organic matter in the regolith (see table A2). According to these calculations, 67% ± 63, 27% ± 82 and 65% ± 49 of the fractionated Si (that is Si in clay or biomass) is eroded as Si bound to organic matter for the Alps, Sri Lanka and the Sierra Nevada field sites, respectively. Thus – despite the difficulties in defining τ_{prim}^{Si} or the silicon isotope fractionation factors – this approach supports the conclusion of the coupled Ge/Si-δ^{30}Si mass-balance model in the main text: that Si incorporated into biogenic material is an important silicon export vector in small catchments.

REFERENCES

Aguirre, A. A., ms, 2019, Applying Ge/Si Ratios to Trace Weathering Reactions, Hydrologic Pathways and Coal Fly Ash Contamination in Watersheds Across the United States: Ithaca, New York, Cornell University, Ph. D. thesis, 210 p.

Aguirre, A. A., Derry, L. A., Mills, T. J., and Anderson, S. P., 2017, Colloidal transport in the Gordon Gulch catchment of the Boulder Creek CZO and its effect on C-Q relationships for silicon: Water Resources Research, v. 53, p. 2368–2383, https://doi.org/10.1002/2016WR019730

Alexandre, A., Meunier, J. D., Colin, F., and Koud, J. M., 1997, Plant impact on the biogeochemical cycle of silicon and related weathering processes: Geochimica et Cosmochimica Acta, v. 61, n. 3, p. 677–682, https://doi.org/10.1016/S0016-7037(97)00001-X

Ameijeiras-Mariño, Y., Opfergelt, S., Derry, L. A., Robinet, J., Govers, G., Minella, J. P. G., and Delmelle, P., 2018, Ge/Si ratios point to increased contribution from deeper mineral weathering to streams after forest conversion to cropland: Applied Geochemistry, v. 96, p. 24–34, https://doi.org/10.1016/j.apgeochem.2018.06.002

Anders, A. M., Sletten, R. S., Derry, L. A., and Hallet, B., 2003, Germanium/silicon ratios in the Copper River Basin, Alaska: Weathering and partitioning in periglacial versus glacial environments: Journal of Geophysical Research: Earth Surface, v. 108, n. F1, https://doi.org/10.1029/2003JF000026

Baronas, J. J., Torres, M. A., West, A. J., Rouxel, O., Georg, B., Bouchez, J., Gaillardet, J., and Hammond, D. E., 2018, Ge and Si isotope signatures in rivers: A quantitative multi-proxy approach: Earth and Planetary Science Letters, v. 503, p. 194–215, https://doi.org/10.1016/j.epsl.2018.09.022

Baronas, J. J., West, A. J., Burton, K. W., Hammond, D. E., Opfergelt, S., Pogge von Strandmann, P. A. E., James, R. H., and Rouxel, O. J., 2020, Ge and Si isotope behavior during intense tropical weathering and ecosystem cycling: Global Biogeochemical Cycles, v. 34, n. 8, p. e2019GB006522, https://doi.org/10.1029/2019GB006522

Bateman, P. C., and Wones, D. R., 1972, Huntington Lake Quadrangle, central Sierra Nevada, California; analytic data: USGS Professional Paper 724-A, https://doi.org/10.3133/pp724A

Bayon, G., Delvigne, C., Ponzevera, E., Borges, A., Darchambeau, F., De Deckker, P., Lambert, T., Monin, L., Toucanne, S., and André, L., 2018, The silicon isotopic composition of fine-grained river sediments and its relation to climate and lithology: Geochimica et Cosmochimica Acta, v. 229, p. 147–161, https://doi.org/10.1016/j.gca.2018.03.015

Beattie, P., Drake, M., Jones, J., Leeman, W., Longhi, J., McKay, G., Nielsen, R., Palme, H., Shaw, D., Takahashi, E., and Watson, B., 1993, Terminology for trace-element partitioning: Geochimica et Cosmochimica Acta, v. 57, n. 7, p. 1605–1606, https://doi.org/10.1016/0016-7037(93)90015-O

Behrens, R., Bouchez, J., Schuessler, J. A., Dultz, S., Hewawasam, T., and von Blanckenburg, F., 2015, Mineralogical transformations set slow weathering rates in low-porosity metamorphic bedrock on mountain slopes in a tropical climate: Chemical Geology, v. 411, p. 283–298, https://doi.org/10.1016/j.chemgeo.2015.07.008

Berner, R. A., Lasaga, A. C., and Garrels, R. M., 1983, The carbonate-silicate geochemical cycle and its effect on atmospheric carbon dioxide over the past 100 million years: American Journal of Science, v. 283, n. 7, p. 641–683, https://doi.org/10.2475/ajs.283.7.641

Bernstein, L. R., 1985, Germanium geochemistry and mineralogy: Geochimica et Cosmochimica Acta, v. 49, n. 11, p. 2409–2422, https://doi.org/10.1016/0016-7037(85)90241-8

Beusen, A. H. W., Bouwman, A. F., Dürr, H. H., Dekkers, A. L. M., and Hartmann, J., 2009, Global patterns of dissolved silica export to the coastal zone: Results from a spatially explicit global model: Global Biogeochemical Cycles, v. 23, n. 4, p. GB0A02, https://doi.org/10.1029/2008GB003281

Blecker, S. W., King, S. L., Derry, L. A., Chadwick, O. A., Ippolito, J. A., and Kelly, E. F., 2007, The ratio of germanium to silicon in plant phytoliths: Quantification of biological discrimination under controlled experimental conditions: Biogeochemistry, v. 86, p. 189–199, https://doi.org/10.1007/s10533-007-9154-7

Blecker, S., ms. 2005, Silica biogeochemistry across the Great Plains: Fort Collins, Colorado, Colorado State University, Colorado State University, Ph. D. thesis, 156 p.

Bouchez, J., and von Blanckenburg, F., 2021, The role of vegetation in setting strontium stable isotope ratios in the Critical Zone: American Journal of Science, v. 321, n. 8, p. 1246–1283, https://doi.org/10.2475/08.2021.04

Bouchez, J., Lupker, M., Gaillardet, J., France-Lanord, C., and Maurice, L., 2011, How important is it to integrate riverine suspended sediment chemical composition with depth? Clues from Amazon River depth-profiles: Geochimica et Cosmochimica Acta, v. 75, n. 22, p. 6955–6970, https://doi.org/10.1016/j.gca.2011.08.038

Bouchez, J., von Blanckenburg, F., and Schuessler, J. A., 2013, Modeling novel stable isotope ratios in the weathering zone: American Journal of Science, v. 313, n. 4, p. 267–308, https://doi.org/10.2475/04.2013.01

Brantley, S. L., Goldhaber, M. B., and Ragnarsdottir, K. V., 2007, Crossing disciplines and scales to understand the critical zone: Elements, v. 3, n. 5, p. 307–314, https://doi.org/10.2113/gselements.3.5.307

Brimhall, G. H., and Dietrich, W. E., 1987, Constitutive mass balance relations between chemical composition, volume, density, porosity, and strain in metasomatic hydrochemical systems: Results on weathering and pedogenesis: Geochimica et Cosmochimica Acta, v. 51, n. 3, p. 567–587, https://doi.org/10.1016/0016-7037(87)90070-6

Bunte, K., Swingle, K. W., Turowski, J. M., Abt, S. R., and Cenderelli, D. A., 2016, Measurements of coarse particulate organic matter transport in steep mountain streams and estimates of decadal CPOM exports: Journal of Hydrology, v. 539, p. 162–176, https://doi.org/10.1016/j.jhydrol.2016.05.022

Carbonnel, V., Lionard, M., Muylaert, K., and Chou, L., 2009, Dynamics of dissolved and biogenic silica in the freshwater reaches of a macrotidal estuary (The Scheldt, Belgium): Biogeochemistry, v. 96, p. 49–72, https://doi.org/10.1007/s10533-009-9344-6

Carey, J. C., and Fulweiler, R. W., 2012, The Terrestrial Silica Pump: PLoS ONE, v. 7, p. e52932, https://doi.org/10.1371/journal.pone.0052932

Cary, L., Alexandre, A., Meunier, J. D., Boeglin, J. L., and Braun, J. J., 2005, Contribution of phytoliths to the suspended load of biogenic silica in the Nyong basin rivers (Cameroon): Biogeochemistry, v. 74, p. 101–114, https://doi.org/10.1007/s10533-004-2945-1

Clymans, W., Conley, D. J., Battles, J. J., Frings, P. J., Koppers, M. M., Likens, G. E., and Johnson, C. E., 2016, Silica uptake and release in live and decaying biomass in a northern hardwood forest: Ecology, v. 97, n. 11, p. 3044–3057, https://doi.org/10.1002/ecy.1542

Clymans, W., Govers, G., Frot, E., Ronchi, B., Van Wesemael, B., and Struyf, E., 2013, Temporal dynamics of bio-available Si fluxes in a temperate forested catchment (Meerdaal forest, Belgium): Biogeochemistry, v. 116, p. 275–291, https://doi.org/10.1007/s10533-013-9858-9

Clymans, W., Struyf, E., Van den Putte, A., Langhans, C., Wang, Z., and Govers, G., 2015, Amorphous silica mobilization by inter-rill erosion: Insights from rainfall experiments: Earth Surface Processes and Landforms, v. 40, n. 9https://doi.org/10.1002/esp.3707

Conley, D. J., 1997, Riverine contribution of biogenic silica to the oceanic silica budget: Limnology and Oceanography, v. 42, n. 4, p. 774–777, https://doi.org/10.4319/lo.1997.42.4.0774

Conley, D. J., 2002, Terrestrial ecosystems and the global biogeochemical silica cycle: Global Biogeochemical Cycles, v. 16, n. 4, p. 112, https://doi.org/10.1029/2002GB001894

Coplen, T. B., 2011, Guidelines and recommended terms for expression of stable-isotope-ratio and gas-ratio measurement results: Rapid Communications in Mass Spectrometry, v. 25, n. 17, p. 2538–2560, https://doi.org/10.1002/rcm.5129

Cornelis, J. T., Delvaux, B., Cardinal, D., André, L., Ranger, J., and Opfergelt, S., 2010, Tracing mechanisms controlling the release of dissolved silicon in forest soil solutions using Si isotopes and Ge/Si ratios: Geochimica et Cosmochimica Acta, v. 74, n. 14, p. 3913–3924, https://doi.org/10.1016/j.gca.2010.04.056

Criss, R. E., 1999, Principles of stable isotope distribution: New York, Oxford, Oxford University Press, 254 p., https://doi.org/10.1093/oso/9780195117752.001.0001

Dahlgren, R. A., Boettinger, J. L., Huntington, G. L., and Amundson, R. G., 1997, Soil development along an elevational transect in the western Sierra Nevada, California: Geoderma, v. 78, n. 3–4, p. 207–236, https://doi.org/10.1016/S0016-7061(97)00034-7

De Argollo, R., and Schilling, J.-G., 1978, Ge-Si and Ga-Al fractionation in Hawaiian volcanic rocks: Geochimica et Cosmochimica Acta, v. 42, n. 6, Part A, p. 623–630, https://doi.org/10.1016/0016-7037(78)90007-8

De La Rocha, C. L., Brzezinski, M. A., and DeNiro, M. J., 2000, A first look at the distribution of the stable isotopes of silicon in natural waters: Geochimica et Cosmochimica Acta, v. 64, n. 14, p. 2467–2477, https://doi.org/10.1016/S0016-7037(00)00373-2

de Oliveira Garcia, W., Amann, T., and Hartmann, J., 2018, Increasing biomass demand enlarges negative forest nutrient budget areas in wood export regions: Scientific Reports, v. 8, article number 5280, https://doi.org/10.1038/s41598-018-22728-5

de Tombeur, F., Turner, B. L., Laliberté, E., Lambers, H., Mahy, G., Faucon, M.-P., Zemunik, G., and Cornelis, J.-T., 2020, Plants sustain the terrestrial silicon cycle during ecosystem retrogression: Science, v. 369, n. 6508, p. 1245–1248, https://doi.org/10.1126/science.abc0393

Dellinger, M., Gaillardet, J., Bouchez, J., Calmels, D., Louvat, P., Dosseto, A., Gorge, C., Alanoca, L., and Maurice, L., 2015, Riverine Li isotope fractionation in the Amazon River basin controlled by the weathering regimes: Geochimica et Cosmochimica Acta, v. 164, p. 71–93, https://doi.org/10.1016/j.gca.2015.04.042

Delvigne, C., Angeletti, B., Guihou, A., and Basile-Doelsch, I., and Meunier, J. D., 2018, Reliable determination of Ge in solid nvironmental samples using a chemical preparation procedure developed for Si isotopes and ICP-MS Analysis: Geostandards and Geoanalytical Research, v. 42, n. 1, p. 139–149, https://doi.org/10.1111/ggr.12197

Delvigne, C., Opfergelt, S., Cardinal, D., Delvaux, B., and André, L., 2009, Distinct silicon and germanium pathways in the soil-plant system: Evidence from banana and horsetail: Journal of Geophysical Research-Biogeosciences, v. 114, n. G2, p. 11, https://doi.org/10.1029/2008JG000899

Derry, L. A., Kurtz, A. C., Ziegler, K., and Chadwick, O. A., 2005, Biological control of terrestrial silica cycling and export fluxes to watersheds: Nature, v. 433, p. 728–731, https://doi.org/10.1038/nature03299

Dietzel, M., 2002, Interaction of polysilicic and monosilicic acid with mineral surfaces: Dordrecht, The Netherlands, Springer, Water Science and Technology Library, v. 40, p. 207–235, https://doi.org/10.1007/978-94-010-0438-1_9

Dinis, P. A., Garzanti, E., Hahn, A., Vermeesch, P., and Cabral-Pinto, M., 2019, Weathering indices as climate proxies. A step forward based on Congo and SW African river muds: Earth-Science Reviews, v. 201, p. 103039, https://doi.org/10.1016/j.earscirev.2019.103039

Dixon, J. L., Heimsath, A. M., and Amundson, R., 2009, The critical role of climate and saprolite weathering in landscape evolution: Earth Surface Processes and Landforms, v. 34, n. 11, p. 1507–1521, https://doi.org/10.1002/esp.1836

Drever, J. I., and Zobrist, J., 1992, Chemical weathering of silicate rocks as a function of elevation in the southern Swiss Alps: Geochimica et Cosmochimica Acta, v. 56, n. 8, p. 3209–3216, https://doi.org/10.1016/0016-7037(92)90298-W

Egli, M., Mirabella, A., and Fitze, P., 2001, Clay mineral formation in soils of two different chronosequences in the Swiss Alps: Geoderma, v. 104, n. 1–2, p. 145–175, https://doi.org/10.1016/S0016-7061(01)00079-9

Egli, M., Mirabella, A., and Sartori, G., 2008, The role of climate and vegetation in weathering and clay mineral formation in late Quaternary soils of the Swiss and Italian Alps: Geomorphology, v. 102, n. 3–4, p. 307–324, https://doi.org/10.1016/j.geomorph.2008.04.001

Evans, M. J., and Derry, L. A., 2002, Quartz control of high germanium/silicon ratios in geothermal waters: Geology, v. 30, n. 11, p. 1019–1022, https://doi.org/10.1130/0091-7613(2002)030<1019:QCOHGS>2.0.CO;2

Filippelli, G. M., Carnahan, J. W., Derry, L. A., and Kurtz, A., 2000, Terrestrial paleorecords of Ge/Si cycling derived from lake diatoms: Chemical Geology, v. 168, n. 1–2, p. 9–26, https://doi.org/10.1016/S0009-2541(00)00185-6

Frings, P. J., 2019, Palaeoweathering: How Do Weathering Rates Vary with Climate?: Elements, v. 15, n. 4, p. 259–265, https://doi.org/10.2138/gselements.15.4.259

Frings, P. J., Clymans, W., and Conley, D. J., 2014, Amorphous Silica Transport in the Ganges Basin: Implications for Si Delivery to the Oceans: Procedia Earth and Planetary Science, v. 10, p. 271–274, https://doi.org/10.1016/j.proeps.2014.08.059

Frings, P. J., Clymans, W., Fontorbe, G., Gray, W., Chakrapani, G. J., Conley, D. J., and De La Rocha, C., 2015, Silicate weathering in the Ganges alluvial plain: Earth and Planetary Science Letters, v. 427, p. 136–148, https://doi.org/10.1016/j.epsl.2015.06.049

Frings, P. J., Fontorbe, G., Clymans, W., De La Rocha, C. L., and Conley, D. J., 2016, The continental Si cycle and its impact on the ocean Si isotope budget: Chemical Geology, v. 425, p. 12–36, https://doi.org/10.1016/j.chemgeo.2016.01.020

Frings, P. J., Oelze, M., Schubring, F., Frick, D. A., and von Blanckenburg, F., 2021a, Interpreting silicon isotopes in the Critical Zone: American Journal of Science, v. 321, n. 8, p. 1164–1203, https://doi.org/10.2475/08.2021.02

Frings, P. J., Oelze, M., Frick, D. A., and von Blanckenburg, F., 2021b, Geochemical data on silicon isotope and Ge/Si ratios along a global erodosequence: GFZ Data Services, https://doi.org/10.5880/GFZ.3.3.2021.003

Froelich, P. N., Blanc, V., Mortlock, R. A., Chillrud, S. N., Dunstan, W., Udomkit, A., and Peng, T. H., 1992, River fluxes of dissolved silica to the ocean were higher during glacials: Ge/Si in diatoms, rivers, and oceans: Paleoceanography and Paleoclimatology, v. 7, n. 6, p. 739–767, https://doi.org/10.1029/92PA02090

Froelich, P. N., Hambrick, G. A., Andreae, M. O., Mortlock, R. A., and Edmond, J. M., 1985, The geochemistry of inorganic germanium in natural waters: Journal of Geophysical Research: Oceans (1978–2012), v. 90, n. C1, p. 1133–1141, https://doi.org/10.1029/JC090iC01p01133

Georg, R. B., Reynolds, B. C., Frank, M., and Halliday, A. N., 2006, New sample preparation techniques for the determination of Si isotopic compositions using MC-ICPMS: Chemical Geology, v. 235, n. 1–2, p. 95–104, https://doi.org/10.1016/j.chemgeo.2006.06.006

Gerard, F., Mayer, K. U., Hodson, M. J., and Ranger, J., 2008, Modelling the biogeochemical cycle of silicon in soils: Application to a temperate forest ecosystem: Geochimica et Cosmochimica Acta, v. 72, n. 3, p. 741–758, https://doi.org/10.1016/j.gca.2007.11.010

Goldschmidt, V. M., 1926, Concerning the crystallo-chemical and geochemical behaviour of Germanium: Naturwissenschaften, v. 14, p. 295–297, https://doi.org/10.1007/BF01503585

Guntzer, F., Keller, C., and Meunier, J.-D., 2012, Benefits of plant silicon for crops: A review: Agronomy for Sustainable Development, v. 32, p. 201–213, https://doi.org/10.1007/s13593-011-0039-8

Hayes, J. M., 2004, An introduction to isotopic calculations: Woods Hole, Massachusetts, Woods Hole Oceanographic Institute, 10 p.

Hewawasam, T., von Blanckenburg, F., Bouchez, J., Dixon, J. L., Schuessler, J. A., and Maekeler, R., 2013, Slow advance of the weathering front during deep, supply-limited saprolite formation in the tropical Highlands of Sri Lanka: Geochimica et Cosmochimica Acta, v. 118, p. 202–230, https://doi.org/10.1016/j.gca.2013.05.006

Hodson, M. J., 2016, The development of phytoliths in plants and its influence on their chemistry and isotopic composition. Implications for palaeoecology and archaeology: Journal of Archaeological Science, v. 68, p. 62–69, https://doi.org/10.1016/j.jas.2015.09.002

Hodson, M. J., 2019, The relative importance of cell wall and lumen phytoliths in carbon sequestration in soil: A hypothesis: Frontiers in Earth Science, v. 7, https://doi.org/10.3389/feart.2019.00167

Hughes, H. J., Sondag, F., Santos, R. V., André, L., and Cardinal, D., 2013, The riverine silicon isotope composition of the Amazon Basin: Geochimica et Cosmochimica Acta, v. 121, p. 637–651, https://doi.org/10.1016/j.gca.2013.07.040

Hunsaker, C. T., and Neary, D. G., 2012, Sediment loads and erosion in forest headwater streams of the Sierra Nevada, California , *in* Revisiting Experimental Catchment Studies in Forest Hydrology: Proceedings of a workshop for the International Association of Hydrological Sciences, General Assembly in Melbourne: Wallingford, United Kingdom, IAHS Publication 353, p. 195–204.

Jochum, K. P., Nohl, U., Herwig, K., Lammel, E., Stoll, B., and Hofmann, A. W., 2005, GeoReM: A New Geochemical Database for Reference Materials and Isotopic Standards: Geostandards and Geoanalytical Research, v. 29, n. 3, p. 333–338, https://doi.org/10.1111/j.1751-908X.2005.tb00904.x

Jung, M., Koirala, S., Weber, U., Ichii, K., Gans, F., Camps-Valls, G., Papale, D., Schwalm, C., Tramontana, G., and Reichstein, M., 2019, The FLUXCOM ensemble of global land-atmosphere energy fluxes: Scientific data, v. 6, p. 74, https://doi.org/10.1038/s41597-019-0076-8

Kaiser, S., Wagner, S., Moschner, C., Funke, C., and Wiche, O., 2020, Accumulation of germanium (Ge) in plant tissues of grasses is not solely driven by its incorporation in phytoliths: Biogeochemistry, v. 148, p. 49–68, https://doi.org/10.1007/s10533-020-00646-x

Kim, H., Gu, X., and Brantley, S. L., 2018, Particle fluxes in groundwater change subsurface shale rock chemistry over geologic time: Earth and Planetary Science Letters, v. 500, p. 180–191, https://doi.org/10.1016/j.epsl.2018.07.031

Klotzbücher, T., Klotzbücher, A., Kaiser, K., Merbach, I., and Mikutta, R., 2018, Impact of agricultural practices on plant-available silicon: Geoderma, v. 331, p. 15–17, https://doi.org/10.1016/j.geoderma.2018.06.011

Kramer, N., Wohl, E., and Hess-Homeier, B., and Leisz, S., 2017, The pulse of driftwood export from a very large forested river basin over multiple time scales, Slave River, Canada: Water Resources Research, v. 53, n. 3, p. 1928–1947, https://doi.org/10.1002/2016WR019260

Kurtz, A. C., Derry, L. A., and Chadwick, O. A., 2002, Germanium-silicon fractionation in the weathering environment: Geochimica et Cosmochimica Acta, v. 66, n. 9, p. 1525–1537, https://doi.org/10.1016/S0016-7037(01)00869-9

Kurtz, A. C., Lugolobi, F., and Salvucci, G., 2011, Germanium-silicon as a flow path tracer: Application to the Rio Icacos watershed: Water Resources Research, v. 47, n. 6, p. W06516, https://doi.org/10.1029/2010WR009853

Kurtz, A., and Derry, L., 2004, Tracing silicate weathering and terrestrial silica cycling with Ge/Si ratios , in Wanty, R. B., and Seal, R. R., editors, 11th International Symposium on Water Rock Interaction: Lisse, The Netherlands, Swets and Zeitlinger Publications, p. 833–836.

Lebedeva, M. I., Fletcher, R. C., and Brantley, S. L., 2010, A mathematical model for steady-state regolith production at constant erosion rate: Earth Surface Processes and Landforms: The Journal of the British Geomorphological Research Group, v. 35, n. 5, p. 508–524, https://doi.org/10.1002/esp.1954

Lee, H., Galy, V., Feng, X., Ponton, C., Galy, A., France-Lanord, C., and Feakins, S. J., 2019, Sustained wood burial in the Bengal Fan over the last 19 My: Proceedings of the National Academy of Sciences of the United States of America, v. 116, n. 45, p. 22518–22525, https://doi.org/10.1073/pnas.1913714116

Li, Z., Cornelis, J.-T., Linden, C. V., Van Ranst, E., and Delvaux, B., 2020, Neoformed aluminosilicate and phytogenic silica are competitive sinks in the silicon soil–plant cycle: Geoderma, v. 368, p. 114308, https://doi.org/10.1016/j.geoderma.2020.114308

Liu, F., Hunsaker, C., and Bales, R. C., 2013, Controls of streamflow generation in small catchments across the snow–rain transition in the Southern Sierra Nevada, California: Hydrological Processes, v. 27, n. 14, p. 1959–1972, https://doi.org/10.1002/hyp.9304

Liu, J., Zang, J., Bouwman, L., Liu, S., Yu, Z., and Ran, X., 2016, Distribution and budget of dissolved and biogenic silica in the Bohai Sea and Yellow Sea: Biogeochemistry, v. 130, p. 85–101, https://doi.org/10.1007/s10533-016-0244-2

Lucas, Y., 2001, The role of plants in controlling rates and products of weathering: Importance of biological pumping: Annual Review of Earth and Planetary Sciences, v. 29, p. 135–163, https://doi.org/10.1146/annurev.earth.29.1.135

Lugolobi, F., Kurtz, A. C., and Derry, L. A., 2010, Germanium-silicon fractionation in a tropical, granitic weathering environment: Geochimica et Cosmochimica Acta, v. 74, n. 4, p. 1294–1308, https://doi.org/10.1016/j.gca.2009.11.027

Ma, J. F., Miyake, Y., and Takahashi, E., 2001, Silicon as a beneficial element for crop plants , *in* Datnoff, L. E., Snyder, G. H., and Korndörfer, G. H., editors, Silicon in Agriculture: London, Elsevier, Studies in Plant Science, v. 8, p. 17–39, https://doi.org/10.1016/S0928-3420(01)80006-9

Martin, F., Ildefonse, P., Hazemann, J.-L., Petit, S., Grauby, O., and Decarreau, A., 1996, Random distribution of Ge and Si in synthetic talc: An EXAFS and FTIR study, https://doi.org/10.1127/ejm/8/2/0289

Meek, K., Derry, L., Sparks, J., and Cathles, L., 2016, $^{87}Sr/^{86}Sr$, Ca/Sr, and Ge/Si ratios as tracers of solute sources and biogeochemical cycling at a temperate forested shale catchment, central Pennsylvania, USA: Chemical Geology, v. 445, p. 84–102, https://doi.org/10.1016/j.chemgeo.2016.04.026

Meunier, J. D., Colin, F., and Alarcon, C., 1999, Biogenic silica storage in soils: Geology, v. 27, n. 9, p. 835–838, https://doi.org/10.1130/0091-7613(1999)027<0835:BSSIS>2.3.CO;2

Meunier, J.-D., Riotte, J., Braun, J.-J., Sekhar, M., Chalié, F., Barboni, D., and Saccone, L., 2015, Controls of DSi in streams and reservoirs along the Kaveri River, South India: Science of The Total Environment, v. 502, p. 103–113, https://doi.org/10.1016/j.scitotenv.2014.07.107

Mortlock, R. A., and Froelich, P. N., 1987, Continental weathering of germanium – Ge/Si in the global river discharge: Geochimica et Cosmochimica Acta, v. 51, n. 8, p. 2075–2082, https://doi.org/10.1016/0016-7037(87)90257-2

Mortlock, R. A., and Froelich, P. N., 1996, Determination of germanium by isotope dilution-hydride generation inductively coupled plasma mass spectrometry: Analytica Chimica Acta, v. 332, n. 2–3, p. 277–284, https://doi.org/10.1016/0003-2670(96)00230-9

Murnane, R. J., and Stallard, R. F., 1990, Germanium and silicon in rivers of the Orinoco drainage-basin: Nature, v. 344, p. 749–752, https://doi.org/10.1038/344749a0

Nesbitt, H. W., and Young, G. M., 1982, Early Proterozoic climates and plate motions inferred from major element chemistry of lutites: Nature, v. 299, p. 715–717, https://doi.org/10.1038/299715a0

Norton, K. P., and von Blanckenburg, F., 2010, Silicate weathering of soil-mantled slopes in an active Alpine landscape: Geochimica et Cosmochimica Acta, v. 74, n. 18, p. 5243–5258, https://doi.org/10.1016/j.gca.2010.06.019

Norton, K. P., von Blanckenburg, F., and Kubik, P. W., 2010, Cosmogenic nuclide-derived rates of diffusive and episodic erosion in the glacially sculpted upper Rhone Valley, Swiss Alps: Earth Surface Processes and Landforms, v. 35, n. 6, p. 651–662, https://doi.org/10.1002/esp.1961

Novokahatskiy, I. P., and Kalinin, S. K., And Zamyatina, G. M., 1967, Germanium content of igneous and altered rocks of Kazakhstan: Geochemistry International USSR, v. 4, p. 1192–1196.

Oeser, R. A., and von Blanckenburg, F., 2020, Strontium isotopes trace biological activity in the Critical Zone along a climate and vegetation gradient: Chemical Geology, v. 558, p. 119861, https://doi.org/10.1016/j.chemgeo.2020.119861

Opfergelt, S., and Delmelle, P., 2012, Silicon isotopes and continental weathering processes: Assessing controls on Si transfer to the ocean: Comptes Rendus Geoscience, v. 344, n. 11–12, p. 723–738, https://doi.org/10.1016/j.crte.2012.09.006

Opfergelt, S., Cardinal, D., André, L., Delvigne, C., Bremond, L., and Delvaux, B., 2010, Variations of $\delta^{30}Si$ and Ge/Si with weathering and biogenic input in tropical basaltic ash soils under monoculture: Geochimica et Cosmochimica Acta, v. 74, n. 1, p. 225–240, https://doi.org/10.1016/j.gca.2009.09.025

Parr, J. F., Dolic, V., Lancaster, G., and Boyd, W. E., 2001, A microwave digestion method for the extraction of phytoliths from herbarium specimens: Review of Palaeobotany and Palynology, v. 116, p. 203–212, https://doi.org/10.1016/S0034-6667(01)00089-6

Perez-Fodich, A., and Derry, L. A., 2020, A model for germanium-silicon equilibrium fractionation in kaolinite: Geochimica et Cosmochimica Acta, v. 288, p. 199–213, https://doi.org/10.1016/j.gca.2020.07.046

Pilon-Smits, E. A. H., Quinn, C. F., Tapken, W., Malagoli, M., and Schiavon, M., 2009, Physiological functions of beneficial elements: Current Opinion in Plant Biology, v. 12, n. 3, p. 267–274, https://doi.org/10.1016/j.pbi.2009.04.009

Pokrovski, G. S., and Schott, J., 1998, Experimental study of the complexation of silicon and germanium with aqueous organic species: Implications for germanium and silicon transport and Ge/Si ratio in natural waters: Geochimica et Cosmochimica Acta, v. 62, n. 21–22, p. 3413–3428, https://doi.org/10.1016/S0016-7037(98)00249-X

Pokrovsky, O., Pokrovski, G., Schott, J., and Galy, A., 2006, Experimental study of germanium adsorption on goethite and germanium coprecipitation with iron hydroxide: X-ray absorption fine structure and macroscopic characterization: Geochimica et Cosmochimica Acta, v. 70, n. 13, p. 3325–3341, https://doi.org/10.1016/j.gca.2006.04.012

Prieto, M., 2009, Thermodynamics of solid solution-aqueous solution systems: Reviews in Mineralogy and Geochemistry, v. 70, p. 47–85, https://doi.org/10.2138/rmg.2009.70.2

Rains, D. W., Epstein, E., Zasoski, R. J., and Aslam, M., 2006, Active silicon uptake by wheat: Plant and Soil, v. 280, p. 223–228, https://doi.org/10.1007/s11104-005-3082-x

Ran, X., Liu, S., Liu, J., Zang, J., Che, H., Ma, Y., and Wang, Y., 2016, Composition and variability in the export of biogenic silica in the Changjiang River and the effect of Three Gorges Reservoir: Science of The Total Environment, v. 571, p. 1191–1199, https://doi.org/10.1016/j.scitotenv.2016.07.125

Riebe, C. S., Kirchner, J. W., and Finkel, R. C., 2003, Long-term rates of chemical weathering and physical erosion from cosmogenic nuclides and geochemical mass balance: Geochimica et Cosmochimica Acta, v. 67, n. 22, p. 4411–4427, https://doi.org/10.1016/S0016-7037(03)00382-X

Sangster, A. G., Hodson, M. J., and Tubb, H. J., 2001, Silicon deposition in higher plants : The Netherlands, Elsevier, Studies in Plant Science, v. 8, p. 85–113, https://doi.org/10.1016/S0928-3420(01)80009-4

Sauer, D., Saccone, L., Conley, D. J., Herrmann, L., and Sommer, M., 2006, Review of methodologies for extracting plant-available and amorphous Si from soils and aquatic sediments: Biogeochemistry, v. 80, p. 89–108, https://doi.org/10.1007/s10533-005-5879-3

Savage, P. S., Armytage, R. M. G., Georg, R. B., and Halliday, A. N., 2014, High temperature silicon isotope geochemistry: Lithos, v. 190–191, p. 500–519, https://doi.org/10.1016/j.lithos.2014.01.003

Savage, P. S., Georg, R. B., Williams, H. M., and Halliday, A. N., 2013a, The silicon isotope composition of the upper continental crust: Geochimica et Cosmochimica Acta, v. 109, p. 384–399, https://doi.org/10.1016/j.gca.2013.02.004

Savage, P. S., Georg, R. B., Williams, H. M., and Halliday, A. N., 2013b, Silicon isotopes in granulite xenoliths: Insights into isotopic fractionation during igneous processes and the composition of the deep continental crust: Earth and Planetary Science Letters, v. 365, p. 221–231, https://doi.org/10.1016/j.epsl.2013.01.019

Savage, P. S., Georg, R. B., Williams, H. M., Turner, S., Halliday, A. N., and Chappell, B. W., 2012, The silicon isotope composition of granites: Geochimica et Cosmochimica Acta, v. 92, p. 184–202, https://doi.org/10.1016/j.gca.2012.06.017

Schoelynck, J., Subalusky, A. L., Struyf, E., Dutton, C. L., Unzué-Belmonte, D., Van de Vijver, B., Post, D. M., Rosi, E. J., Meire, P., and Frings, P., 2019, Hippos (*Hippopotamus amphibius*): The animal silicon pump: Science Advances, v. 5, n. 5, p. eaav0395, https://doi.org/10.1126/sciadv.aav0395

Scribner, A. M., Kurtz, A. C., and Chadwick, O. A., 2006, Germanium sequestration by soil: Targeting the roles of secondary clays and Fe-oxyhydroxides: Earth and Planetary Science Letters, v. 243, n. 3–4, p. 760–770, https://doi.org/10.1016/j.epsl.2006.01.051

Sferratore, A., Billen, G., Garnier, J., and Théry, S., 2005, Modeling nutrient (N, P, Si) budget in the Seine watershed: Application of the Riverstrahler model using data from local to global scale resolution: Global Biogeochemical Cycles, v. 19, n. 4, https://doi.org/10.1029/2005GB002496

Smis, A., Van Damme, S., Struyf, E., Clymans, W., Van Wesemael, B., Frot, E., Vandevenne, F., Van Hoestenberghe, T., Govers, G., and Meire, P., 2011, A trade-off between dissolved and amorphous silica transport during peak flow events (Scheldt river basin, Belgium): Impacts of precipitation intensity on terrestrial Si dynamics in strongly cultivated catchments: Biogeochemistry, v. 106, p. 475–487, https://doi.org/10.1007/s10533-010-9527-1

Sommer, M., Kaczorek, D., Kuzyakov, Y., and Breuer, J., 2006, Silicon pools and fluxes in soils and landscapes – a review: Journal of Plant Nutrition and Soil Science-Zeitschrift Fur Pflanzenernahrung Und Bodenkunde, v. 169, n. 3, p. 310–329, https://doi.org/10.1002/jpln.200521981

Sparks, J. P., Chandra, S., Derry, L. A., Parthasarathy, M. V., Daugherty, C. S., and Griffin, R., 2011, Subcellular localization of silicon and germanium in grass root and leaf tissues by SIMS: Evidence for differential and active transport: Biogeochemistry, v. 104, p. 237–249, https://doi.org/10.1007/s10533-010-9498-2

Strömberg, C. A. E., Di Stilio, V. S., and Song, Z., 2016, Functions of phytoliths in vascular plants: An evolutionary perspective: Functional Ecology, v. 30, n. 8, p. 1286–1297, https://doi.org/10.1111/1365-2435.12692

Struyf, E., Smis, A., Van Damme, S., Garnier, J., Govers, G., Van Wesemael, B., Conley, D. J., Batelaan, O., Frot, E., Clymans, W., Vandevenne, F., Lancelot, C., Goos, P., and Meire, P., 2010, Historical land use change has lowered terrestrial silica mobilization: Nature Communications, v. 1, article number 129, https://doi.org/10.1038/ncomms1128

Trembath-Reichert, E., Wilson, J. P., McGlynn, S. E., and Fischer, W. W., 2015, Four hundred million years of silica biomineralization in land plants: Proceedings of the National Academy of Sciences of the United States of America, v. 112, n. 17, p. 5449–5454, https://doi.org/10.1073/pnas.1500289112

Turowski, J. M., Hilton, R. G., and Sparkes, R., 2016, Decadal carbon discharge by a mountain stream is dominated by coarse organic matter: Geology, v. 44, n. 1, p. 27–30, https://doi.org/10.1130/G37192.1

Uhlig, D., Schuessler, J. A., Bouchez, J., Dixon, J. L., and von Blanckenburg, F., 2017, Quantifying nutrient uptake as driver of rock weathering in forest ecosystems by magnesium stable isotopes: Biogeosciences, v. 14, p. 3111–3128, https://doi.org/10.5194/bg-14-3111-2017

Vandevenne, F., Struyf, E., Clymans, W., and Meire, P., 2012, Agricultural silica harvest: Have humans created a new loop in the global silica cycle?: Frontiers in Ecology and the Environment, v. 10, n. 5, p. 243–248, https://doi.org/10.1890/110046

von Blanckenburg, F., Schuessler, J. A., Bouchez, J., Frings, P. J., Uhlig, D., Oelze, M., Frick, D. A., Hewawasam, T., Dixon, J., and Norton, K., 2021, Rock weathering and nutrient cycling along an erodosequence: American Journal of Science, v. 321, n. 8, p. 1111–1163, https://doi.org/10.24.75/08.2021.01

West, A. J., Lin, C.-W., Lin, T.-C., Hilton, R. G., Liu, S.-H., Chang, C.-T., Lin, K.-C., Galy, A., Sparkes, R. B., and Hovius, N., 2011, Mobilization and transport of coarse woody debris to the oceans triggered by an extreme tropical storm: Limnology and Oceanography, v. 56, n. 1, p. 77–85, https://doi.org/10.4319/lo.2011.56.1.0077

White, A. F., Vivit, D. V., Schulz, M. S., Bullen, T. D., Evett, R. R., and Aagarwal, J., 2012, Biogenic and pedogenic controls on Si distributions and cycling in grasslands of the Santa Cruz soil chronosequence, California: Geochimica et Cosmochimica Acta, v. 94, p. 72–94, https://doi.org/10.1016/j.gca.2012.06.009

Wiche, O., Székely, B., Moschner, C., and Heilmeier, H., 2018, Germanium in the soil-plant system—a review: Environmental Science and Pollution Research, v. 25, p. 31938–31956, https://doi.org/10.1007/s11356-018-3172-y

Wickman, F. E., 1943, Some aspects of the geochemistry of igneous rocks and of differentiation by crystallization: Geologiska Föreningen i Stockholm Förhandlingar, v. 65, n. 4, p. 371–396, https://doi.org/10.1080/11035894309447152

Winnick, M. J., and Maher, K., 2018, Relationships between CO_2, thermodynamic limits on silicate weathering, and the strength of the silicate weathering feedback: Earth and Planetary Science Letters, v. 485, p. 111–120, https://doi.org/10.1016/j.epsl.2018.01.005

Wittmann, H., Oelze, M., Gaillardet, J., Garzanti, E., and von Blanckenburg, F., 2020, A global rate of denudation from cosmogenic nuclides in the Earth's largest rivers: Earth-Science Reviews, v. 204, p. 103147, https://doi.org/10.1016/j.earscirev.2020.103147

Wohl, E., Dwire, K., Sutfin, N., Polvi, L., and Bazan, R., 2012, Mechanisms of carbon storage in mountainous headwater rivers: Nature Communications, v. 3, article number 1263, p. 1–8, https://doi.org/10.1038/ncomms2274

Zang, J., Liu, S., Liu, Y., Ma, Y., and Ran, X., 2016, Contribution of phytoliths to total biogenic silica volumes in the tropical rivers of Malaysia and associated implications for the marine biogeochemical cycle: Chinese Journal of Oceanology and Limnology, v. 34, p. 1076–1084, https://doi.org/10.1007/s00343-016-5116-z

Ziegler, K., Chadwick, O. A., Brzezinski, M. A., and Kelly, E. F., 2005a, Natural variations of δ^{30}Si ratios during progressive basalt weathering, Hawaiian Islands: Geochimica et Cosmochimica Acta, v. 69, n. 19, p. 4597–4610, https://doi.org/10.1016/j.gca.2005.05.008

Ziegler, K., Chadwick, O. A., White, A. F., and Brzezinski, M. A., 2005b, δ^{30}Si systematics in a granitic saprolite, Puerto Rico: Geology, v. 33, n. 10, p. 817–820, https://doi.org/10.1130/G21707.1